Fire Dynamics Simulator - Technical Reference Guide

Kevin B. McGrattan
Howard R. Baum
Ronald G. Rehm
Anthony Hamins
Glenn P. Forney

U.S. DEPARTMENT OF COMMERCE
Technology Administration
National Institute of Standards
and Technology
Gaithersburg, MD 20899

Fire Dynamics Simulator - Technical Reference Guide

Kevin B. McGrattan
Howard R. Baum
Ronald G. Rehm
Anthony Hamins
Glenn P. Forney

U.S. DEPARTMENT OF COMMERCE
Technology Administration
National Institute of Standards
and Technology
Gaithersburg, MD 20899

January 2000

Disclaimer

The US Department of Commerce makes no warranty, expressed or implied, to users of the Fire Dynamics Simulator (FDS), and accepts no responsibility for its use. Users of FDS assume sole responsibility under Federal law for determining the appropriateness of its use in any particular application; for any conclusions drawn from the results of its use; and for any actions taken or not taken as a result of analyses performed using these tools.

Users are warned that FDS is intended for use only by those competent in the fields of fluid dynamics, thermodynamics, combustion, and heat transfer, and is intended only to supplement the informed judgment of the qualified user. The software package is a computer model that may or may not have predictive capability when applied to a specific set of factual circumstances. Lack of accurate predictions by the model could lead to erroneous conclusions with regard to fire safety. All results should be evaluated by an informed user.

Throughout this document, the mention of computer hardware or commercial software does not constitute endorsement by NIST, nor does it indicate that the products are necessarily those best suited for the intended purpose.

Contents

1   Introduction

The idea that the dynamics of a fire might be studied numerically dates back to the beginning of the computer age. Indeed, the fundamental conservation equations governing fluid dynamics, heat transfer, and combustion were first written down over a century ago. Despite this, practical mathematical models of fire (as distinct from controlled combustion) are relatively recent due to the inherent complexity of the problem. Indeed, in his brief history of the early days of fire research, Hoyt Hottel noted "A case can be made for fire being, next to the life processes, the most complex of phenomena to understand" [1].

The difficulties revolve about three issues: First, there are an enormous number of possible fire scenarios to consider due to their accidental nature. Second, the physical insight and computing power necessary to perform all the necessary calculations for most fire scenarios are limited. Any fundamentally based study of fires must consider at least some aspects of bluff body aerodynamics, multi-phase flow, turbulent mixing and combustion, radiative transport, and conjugate heat transfer; all of which are active research areas in their own right. Finally, the "fuel" in most fires was never intended as such. Thus, the mathematical models and the data needed to characterize the degradation of the condensed phase materials that supply the fuel may not be available. Indeed, the mathematical modeling of the physical and chemical transformations of real materials as they burn is still in its infancy.

In order to make progress, the questions that are asked have to be greatly simplified. To begin with, instead of seeking a methodology that can be applied to all fire problems, we begin by looking at a few scenarios that seem to be most amenable to analysis. Hopefully, the methods developed to study these "simple" problems can be generalized over time so that more complex scenarios can be analyzed. Second, we must learn to live with idealized descriptions of fires and approximate solutions to our idealized equations. Finally, the methods should be capable of systematic improvement. As our physical insight and computing power grow more powerful, the methods of analysis can grow with them.

To date, three distinct approaches to the simulation of fires have emerged. Each of these treats the fire as an inherently three dimensional process evolving in time. The first to reach maturity, the "zone" models, describe compartment fires. Each compartment is divided into two spatially homogeneous volumes, a hot upper layer and a cool lower layer. Mass and energy balances are enforced for each layer, with additional models describing other physical processes appended as differential or algebraic equations as appropriate. Examples of such phenomena include fire plumes, flows through doors, windows and other vents, radiative and convective heat transfer, and solid fuel pyrolysis. An excellent description of the physical and mathematical assumptions behind the zone modeling concept is given by Quintiere [2], who chronicles developments through 1983. Model development since then has progressed to the point where documented and supported software implementing these models are widely available [3].

The relative physical and computational simplicity of the zone models has led to their widespread use in the analysis of fire scenarios. So long as detailed spatial distributions of physical properties are not required, and the two layer description reasonably approximates reality, these models are quite reliable. However, by their very nature, there is no way to systematically improve them. The rapid growth of computing power and the corresponding maturing of computational fluid dynamics (CFD), has led to the development of CFD based "field" models applied to fire research problems. Virtually all this work is based on the conceptual framework provided by the Reynolds-averaged form of the governing equations, in particular the $k - \varepsilon$ turbulence model pioneered by Patankar and Spalding [4]. The use of CFD models has allowed the description of fires in complex geometries, and the incorporation of a wide variety of physical phenomena. However, these models have a fundamental limitation for fire applications – the averaging procedure at the root of the model equations. The $k - \varepsilon$ model was developed as a time-averaged approximation to the conservation equations of fluid dynamics. While the precise nature of the averaging time is not specified, it is clearly long enough to require the introduction of large eddy transport coefficients to describe the unresolved fluxes of mass, momentum and energy. This is the root cause of the smoothed appearance of the results of

even the most highly resolved fire simulations. The smallest resolvable length scales are determined by the product of the local velocity and the averaging time, rather than the spatial resolution of the underlying computational grid. This property of the $k - \varepsilon$ model is typically exploited in numerical computations by using implicit numerical techniques to take large time steps.

Unfortunately, the evolution of large eddy structures characteristic of most fire plumes is lost with such an approach, as is the prediction of local transient events. It is sometimes argued that the averaging process used to define the equations is an "ensemble average" over many replicates of the same experiment or postulated scenario. However, this is a moot point in fire research since neither experiments nor real scenarios are replicated in the sense required by that interpretation of the equations. The application of "Large Eddy Simulation" (LES) techniques to fire is aimed at extracting greater temporal and spatial fidelity from simulations of fire performed on the more finely meshed grids allowed by ever faster computers. The phrase LES refers to the description of turbulent mixing of the gaseous fuel and combustion products with the local atmosphere surrounding the fire. This process, which determines the burning rate in most fires and controls the spread of smoke and hot gases, is extremely difficult to predict accurately. This is true not only in fire research but in almost all phenomena involving turbulent fluid motion. The basic idea behind the LES technique is that the eddies that account for most of the mixing are large enough to be calculated with reasonable accuracy from the equations of fluid dynamics. The hope (which must ultimately be justified by appeal to experiments) is that small scale eddy motion can either be crudely accounted for or ignored.

The equations describing the transport of mass, momentum, and energy by the fire induced flows must be simplified so that they can be efficiently solved for the fire scenarios of interest. The general equations of fluid dynamics describe a rich variety of physical processes, many of which have nothing to do with fires. Retaining this generality would lead to an enormously complex computational task that would shed very little additional insight on fire dynamics. The simplified equations, developed by Rehm and Baum [5], have been widely adopted by the larger combustion research community, where they are referred to as the "low Mach number" combustion equations. They describe the low speed motion of a gas driven by chemical heat release and buoyancy forces.

The low Mach number equations are solved numerically by dividing the physical space where the fire is to be simulated into a large number of rectangular cells. Within each cell the gas velocity, temperature, *etc.*, are assumed to be uniform; changing only with time. The accuracy with which the fire dynamics can be simulated depends on the number of cells that can be incorporated into the simulation. This number is ultimately limited by the computing power available. Present day desktop computers limit the number of such cells to at most a few million. This means that the ratio of largest to smallest eddy length scales that can be resolved by the computation (the "dynamic range" of the simulation) is roughly $100 \sim 200$. Unfortunately, the range of length scales that need to be accounted for if all relevant fire processes are to be simulated is roughly $10^4 \sim 10^5$ because combustion processes take place at length scales of 1 mm or less, while the length scales associated with building fires are of the order of meters or tens of meters. The form of the numerical equations discussed below depends on which end of the spectrum one wants to capture directly, and which end is to be ignored or approximated.

2 Hydrodynamic Model

An approximate form of the Navier-Stokes equations appropriate for low Mach number applications is used in the model. The approximation involves the filtering out of acoustic waves while allowing for large variations in temperature and density [5]. This gives the equations an elliptic character, consistent with low speed, thermal convective processes. The computation can either be treated as a Direct Numerical Simulation (DNS), in which the dissipative terms are computed directly, or as a Large Eddy Simulation (LES), in which the large scale eddies are computed directly and the sub-grid scale dissipative processes are modeled. The choice of DNS vs. LES depends on the objective of the calculation and the resolution of the computational grid. If, for example, the problem is to simulate the flow of smoke through a large, multi-room enclosure, it is not possible to resolve the combustion and transport processes directly. However, for small-scale combustion experiments, it is possible to compute the transport directly and the combustion processes to some extent.

2.1 Conservation Equations

First, consider the conservation equations of mass, momentum and energy for a thermally-expandable, multi-component mixture of ideal gases [5]:

Conservation of Mass

$$\frac{\partial \rho}{\partial t} + \nabla \cdot \rho \mathbf{u} = 0 \tag{1}$$

Conservation of Species

$$\frac{\partial}{\partial t}(\rho Y_l) + \nabla \cdot \rho Y_l \mathbf{u} = \nabla \cdot (\rho D)_l \nabla Y_l + \dot{W}_l''' \tag{2}$$

Conservation of Momentum

$$\rho \left(\frac{\partial \mathbf{u}}{\partial t} + (\mathbf{u} \cdot \nabla)\mathbf{u} \right) + \nabla p = \rho \mathbf{g} + \mathbf{f} + \nabla \cdot \tau \tag{3}$$

Conservation of Energy

$$\frac{\partial}{\partial t}(\rho h) + \nabla \cdot \rho h \mathbf{u} - \frac{Dp}{Dt} = \dot{q}''' + \nabla \cdot k \nabla T + \nabla \cdot \sum_l h_l (\rho D)_l \nabla Y_l \tag{4}$$

Note that the external force on the fluid, represented by the term $\mathbf{f}$ in Eq. (3), consists of the drag exerted by water droplets emanating from sprinklers. The energy driving the system is represented by the heat release rate $\dot{q}'''$ in Eq. (4). The term $Dp/Dt = \partial p/\partial t + \mathbf{u} \cdot \nabla p$ is a material derivative. All other symbols are listed in the Nomenclature (Section 8).

2.2 State, Mass and Energy Equations

The conservation equations are supplemented by an equation of state relating the thermodynamic quantities density, pressure and enthalpy; ρ, p and h. The pressure is decomposed into three components

$$p = p_0 - \rho_\infty g z + \tilde{p} \tag{5}$$

The first term on the right hand side is the "background" pressure, the second is the hydrostatic contribution, and the third is the flow-induced perturbation pressure. For most applications, p_0 is constant. However, if

the enclosure is tightly sealed, p_0 is allowed to increase (or decrease) with time as the pressure within the enclosure rises due to thermal expansion or falls due to forced ventilation. Also, if the height of the domain is on the order of a kilometer, p_0 can no longer be assumed constant and must be considered a function of the altitude [6].

The purpose of decomposing the pressure is that for low-Mach number flows, it can be assumed that the temperature and density are inversely proportional, and thus the equation of state can be approximated [5]

$$p_0 = \rho T \mathcal{R} \sum (Y_i/M_i) = \rho T \mathcal{R}/M \tag{6}$$

The pressure p in the state and energy equations is replaced by the background pressure p to filter out sound waves that travel at speeds that are much faster than typical flow speeds expected in fire applications. The low Mach number assumption serves two purposes. First, the filtering of acoustic waves means that the time step in the numerical algorithm is bound only by the flow speed as opposed to the speed of sound, and second, the modified state equation leads to a reduction in the number of dependent variables in the system of equations by one. The energy equation (4) is never explicitly solved, but its source terms are included in the expression for the flow divergence, an important quantity in the analysis to follow.

A further assumption about the thermodynamic variables is that the constant-pressure specific heat of the ith species $c_{p,i}$ is assumed to be independent of temperature. Under this assumption, the enthalpy can be written as:

$$h = \sum_l h_l Y_l = T \sum_l c_{p,l} Y_l \tag{7}$$

The specific heat for each species can be expressed in terms of the number of internal degrees of freedom γ active in that molecule.

$$c_{p,l} = \left(\frac{2+\nu_l}{2}\right)\frac{\mathcal{R}}{M_l} = \left(\frac{\gamma_l}{\gamma_l - 1}\right)\frac{\mathcal{R}}{M_l} \tag{8}$$

If the ratio of specific heats γ for each species is assumed to be that of a diatomic molecule ($\nu = 5, \gamma = 7/5$), the equation of state can be rewritten in the form[1]

$$p_0(t) = \frac{\gamma - 1}{\gamma}\rho h \tag{9}$$

Taking the material derivative of Eq. (9) and using the mass and energy conservation equations, the divergence of the velocity field, $\nabla \cdot \mathbf{u}$, can be written in terms of the thermodynamic quantities

$$\nabla \cdot \mathbf{u} = \frac{\gamma - 1}{\gamma p_0}\left(\dot{q}''' + \nabla \cdot k\nabla T + \nabla \cdot \sum_l c_{p,l}T\rho D\nabla Y_l - \frac{1}{\gamma - 1}\frac{dp_0}{dt}\right) \tag{10}$$

If the enclosure is tightly sealed, the background pressure p_0 can no longer be assumed constant due to the increase (or decrease) in mass and thermal energy within the enclosure. The evolution equation for the pressure is found by integrating Eq. (10) over the entire domain Ω

$$\frac{dp_0}{dt} = \frac{\gamma - 1}{V}\left(\int_\Omega \dot{q}''' dV + \int_{\partial\Omega} k\nabla T \cdot d\mathbf{S} + \sum_l \int_{\partial\Omega} c_{p,l}T\rho D\nabla Y_l \cdot d\mathbf{S}\right) - \frac{\gamma p_0}{V}\int_{\partial\Omega}\mathbf{u}\cdot d\mathbf{S} \tag{11}$$

where V is the volume of the enclosure.

---

[1]The basis of this approximation is that nitrogen will be the dominant species in most fire scenarios.

2.3 The Momentum Equation

The momentum equation is simplified by subtracting off the hydrostatic pressure gradient from the momentum equation (3), and then dividing by the density to obtain[2]

$$\frac{\partial \mathbf{u}}{\partial t} + \frac{1}{2}\nabla|\mathbf{u}|^2 - \mathbf{u}\times\omega + \frac{1}{\rho}\nabla\tilde{p} = \frac{1}{\rho}\left((\rho-\rho_\infty)\mathbf{g} + \mathbf{f} + \nabla\cdot\tau\right) \tag{12}$$

To simplify this equation further, a substitution is made

$$\nabla\mathcal{H} \approx \frac{1}{2}\nabla|\mathbf{u}|^2 + \frac{1}{\rho}\nabla\tilde{p} \tag{13}$$

The basis for this approximation is seen in the evolution equation for the circulation, obtained by integrating Eq. (12) over a closed loop moving with the fluid (in the absence of any external force)

$$\frac{d\Gamma}{dt} = \oint \frac{1}{\rho}\left(-\nabla\tilde{p} + (\rho-\rho_\infty)\mathbf{g} + \nabla\cdot\tau\right)\cdot d\mathbf{x} \tag{14}$$

There are three sources of vorticity: the baroclinic torque due to the non-alignment of the density and pressure gradients, buoyancy due to horizontal density gradients, and viscosity. Buoyancy is the dominant source of vorticity, and the approximation above is equivalent to neglecting the baroclinic torque.

Neglecting the baroclinic torque simplifies the elliptic partial differential equation obtained by taking the divergence of the momentum equation

$$\nabla^2\mathcal{H} = -\frac{\partial(\nabla\cdot\mathbf{u})}{\partial t} - \nabla\cdot\mathbf{F} \quad ; \quad \mathbf{F} = -\mathbf{u}\times\omega - \frac{1}{\rho}\left((\rho-\rho_\infty)\mathbf{g} + \mathbf{f} + \nabla\cdot\tau\right) \tag{15}$$

The linear algebraic system arising from the discretization of Eq. (15) has constant coefficients and can be solved to machine accuracy by a fast, direct (*i.e.* non-iterative) method that utilizes fast Fourier transforms. No-flux or forced-flow boundary conditions are specified by asserting that

$$\frac{\partial\mathcal{H}}{\partial n} = -F_n - \frac{\partial u_n}{\partial t} \tag{16}$$

where F_n is the normal component of $\mathbf{F}$ at the vent or solid wall, and $\partial u_n/\partial t$ is the prescribed rate of change in the normal component of velocity at a forced vent. Initially, the velocity is zero everywhere. At open external boundaries the pressure-like term $\mathcal{H}$ is prescribed, depending on whether the flow is outgoing or incoming

$$\begin{aligned}\mathcal{H} &= |\mathbf{u}|^2/2 \quad \text{outgoing}\\ \mathcal{H} &= 0 \qquad\quad \text{incoming}\end{aligned} \tag{17}$$

The outgoing boundary condition assumes that the pressure perturbation $\tilde{p}$ is zero at an outgoing boundary and that $\mathcal{H}$ is constant along streamlines. The incoming boundary condition assumes that $\mathcal{H}$ is zero infinitely far away.

The components of the viscous stress tensor are given by

$$\tau_{ij} = \mu\left(\frac{\partial u_i}{\partial x_j} + \frac{\partial u_j}{\partial x_i} - \delta_{ij}\frac{2}{3}\frac{\partial u_k}{\partial x_k}\right) \tag{18}$$

In the numerical model, there are two options for treating the dynamic viscosity μ. For a Large Eddy Simulation (LES) where the grid resolution is not fine enough to capture the mixing processes at all relevant

---

[2]Note the use of the vector identity $(\mathbf{u}\cdot\nabla)\mathbf{u} = \frac{1}{2}\nabla|\mathbf{u}|^2 - \mathbf{u}\times\omega$.

scales, a sub-grid scale model for the viscosity is applied. Following the analysis of Smagorinsky [7], the viscosity can be modeled as

$$\mu_{\text{LES}} = \max\left(\mu_{\text{DNS}}, \rho\left(C_s\Delta\right)^2 |S|\right) \tag{19}$$

where C_s is an empirical constant, Δ is a length on the order of the size of a grid cell, and $|S|$ is the magnitude of the deformation tensor

$$|S|^2 = 2\left(\frac{\partial u}{\partial x}\right)^2 + 2\left(\frac{\partial v}{\partial y}\right)^2 + 2\left(\frac{\partial w}{\partial z}\right)^2 + \left(\frac{\partial u}{\partial y} + \frac{\partial v}{\partial x}\right)^2 + \left(\frac{\partial u}{\partial z} + \frac{\partial w}{\partial x}\right)^2 + \left(\frac{\partial v}{\partial z} + \frac{\partial w}{\partial y}\right)^2 \tag{20}$$

The thermal conductivity and material diffusivity are related to the turbulent viscosity by

$$k_{\text{LES}} = \frac{\mu_{\text{LES}}\, c_p}{\text{Pr}} \quad ; \quad (\rho D)_{l,\text{LES}} = \frac{\mu_{\text{LES}}}{\text{Sc}} \tag{21}$$

The Prandtl number Pr and the Schmidt number Sc are assumed to be constant for a given scenario.

There have been numerous refinements of the original Smagorinsky model [8, 9, 10], but it is difficult to assess the improvements offered by these newer schemes. There are two reasons for this. First, the structure of the fire plume is so dominated by the large scale resolvable eddies that even a constant eddy viscosity gives results almost identical to those obtained using the Smagorinsky model [11]. Second, the lack of precision in most large scale fire test data makes it difficult to assess the relative accuracy of each model. The Smagorinsky model with constant C_s produces satisfactory results for most large scale applications where boundary layers are not well resolved.

For a Direct Numerical Simulation (DNS), the viscosity, thermal conductivity and material diffusivity are approximated from kinetic theory. The viscosity of the lth species is given by

$$\mu_l = \frac{26.69 \times 10^{-7} (M_l T)^{\frac{1}{2}}}{\sigma_l^2 \Omega_v} \qquad \frac{\text{kg}}{\text{m s}} \tag{22}$$

where σ_l is the Lennard-Jones hard-sphere diameter (Å) and Ω_v is the collision integral, an empirical function of the temperature T. The thermal conductivity of the lth species is given by

$$k_l = \frac{\mu_l\, c_{p,l}}{\text{Pr}} \qquad \frac{\text{W}}{\text{m K}} \tag{23}$$

where the Prandtl number Pr is 0.7. The viscosity and thermal conductivity of a gas mixture are given by

$$\mu_{\text{DNS}} = \sum_l Y_l\, \mu_l \quad ; \quad k_{\text{DNS}} = \sum_l Y_l\, k_l \tag{24}$$

The binary diffusion coefficient of the lth species diffusing into the mth species is given by

$$D_{lm} = \frac{2.66 \times 10^{-7}\, T^{3/2}}{M_{lm}^{\frac{1}{2}}\, \sigma_{lm}^2\, \Omega_D} \qquad \frac{\text{m}^2}{s} \tag{25}$$

where $M_{lm} = 2(1/M_l + 1/M_m)^{-1}$, $\sigma_{lm} = (\sigma_l + \sigma_m)/2$, and Ω_D is the diffusion collision integral, an empirical function of the temperature T [12]. It is assumed that nitrogen is the dominant species in any combustion scenario considered here, thus the diffusion coefficient in the species mass conservation equations is that of the given species diffusing into nitrogen

$$(\rho D)_{l,\text{DNS}} = \rho\, D_{l0} \tag{26}$$

where species 0 is nitrogen.

6

3 Combustion

In the model, the combustion processes are modeled in two ways. In a DNS calculation where the diffusion of fuel and oxygen can be modeled directly, a global one-step, finite-rate chemical reaction is usually used. In cases where the computational grid is not fine enough to resolve the diffusion of fuel and oxygen, Lagrangian particles or "thermal elements" are used to introduce the thermal energy of the fire into the calculation, and also to visualize the movement of the smoke and hot gases. The thermal elements carry the heat released by the fire, providing a self-consistent description of the smoke transport at all resolvable length and time scales.

The terms LES and DNS refer to solution methodologies of the equations of fluid dynamics. The two relatively simple combustion models described below are not inherent to LES or DNS. In fact, the terms "Direct Numerical Simulation" and "Large Eddy Simulation" are more difficult to define when used in the context of a reacting flow calculation.

3.1 Thermal Elements

In an LES calculation, combustion is occuring at length scales well below the resolution limits of the underlying numerical grid, thus the mixing of fuel gases and air cannot be calculated directly. Instead, the fire is represented by discrete Lagrangian particles (or thermal elements) that originate at solid surfaces and release heat at a specified rate. Surfaces heat up due to both convective and radiative heat transfer from some external source, like an ignitor. When a surface heats up to its prescribed ignition temperature, thermal elements are ejected from the surface, and burned at a prescribed rate. The thermal elements are introduced at a rate of $\dot{n}''$ particles per unit time per unit area with a small initial velocity. This initial velocity is a function of the mass loss rate per unit area of the fuel bed, which can be obtained from the heat release rate per unit area $\dot{q}''_f$, the density of the fuel gases ρ_f, and the heat of combustion ΔH

$$u_n = \frac{\dot{q}''_f}{\rho_f \Delta H} \tag{27}$$

The heat release rate of a single thermal element is given by

$$\dot{q}_p = \frac{\dot{q}''_f}{\dot{n}''} \frac{1}{t_b} \qquad (t - t_0 < t_b) \tag{28}$$

where t_b is the burn-out time of the thermal element, and t_0 is the time the element is ejected from the burning surface. A fraction of the energy assigned to each thermal element is emitted as radiation and potentially reabsorbed by surrounding smoke and hot gases. The volumetric heat release rate term in the energy equation is thus given by

$$\dot{q}''' = \frac{\sum_i \dot{q}_{p,i}(1 - \chi_r)}{\delta x \delta y \delta z} + \kappa(\mathbf{x}) \sum_{i=1}^{N_p} \frac{\chi_r \dot{q}_{p,i}}{4\pi|\mathbf{x}_{p,i} - \mathbf{x}|^2} e^{-\int \kappa(l)dl} \tag{29}$$

The first summation is over all active thermal elements in the grid cell whose volume is $\delta x \delta y \delta z$. The second summation is over all other active thermal elements outside of the grid cell whose radiative energy is potentially re-absorbed by the soot contained within the grid cell. The fraction of the elements' energy converted into thermal radiation is constant and given by χ_r. The position of the ith element is $\mathbf{x}_{p,i}$, the heat release rate is $\dot{q}_{p,i}$, and the segment of the line connecting the points $\mathbf{x}_{p,i}$ and $\mathbf{x}$ is given by dl. Since there are hundreds of thousands of thermal elements in a typical calculation, the summation is made over a sampling of the elements that are still burning. The absorption coefficient κ is given by

$$\kappa = 1186 \frac{\rho Y_s T}{\rho_{soot}} \quad \text{m}^{-1} \tag{30}$$

7

where ρY_s is the mass of soot per unit volume and ρ_{soot} is the density of soot itself [13]. More simply, $\rho Y_s / \rho_{soot} \equiv f_v$ the soot volume fraction.

This simple ray-tracing technique to compute the transport of radiant energy from the fire to its surroundings works well in cases where the fire itself is the source of the radiation. However, once walls and the smoke attain temperatures above 400°C, the fire is no longer the sole source of radiation and the use of ray-tracing become more expensive and cumbersome. A better methodology would be to solve the governing equation for thermal radiation directly. An effort is underway to implement this solver.

The heat release rate per unit area $\dot{q}_f''$ is prescribed by the user and is based on experimental measurements for a configuration resembling as much as possible that being modeled. Typically, a calorimetry experiment will produce a time history of the total heat release rate of the fuel array. Dividing the heat release rate by the estimated area of the burning surface yields a time history of the heat release rate per unit area $\dot{q}_f''(t)$. Often this function can be approximated as a constant, but a time-dependent function can also be used in the calculation.

The burn-out time t_b is obtained from the plume correlation of Baum and McCaffrey [14]. It is assumed that a thermal element burns out somewhere in the intermittent region of the plume, $1.32D < z < 3.30D^*$, where z is the height above the fuel surface, $D^* = (\dot{Q}/c_p \rho_\infty T_\infty \sqrt{g})^{2/5}$ is the characteristic diameter of the fire, and $\dot{Q}$ is the total heat release rate of the fire. An estimate of the burn-out time can be made

$$\int_0^{1.32D^*} \frac{dz}{w(z)} < t_b < \int_0^{3.30D^*} \frac{dz}{w(z)} \tag{31}$$

where

$$w(z) = \begin{cases} 2.18\sqrt{gz} & (z < 1.32D^*) & \text{flame region} \\ 2.45\sqrt{gD^*} & (1.32D^* < z < 3.30D^*) & \text{intermittent region} \end{cases} \tag{32}$$

The burn-out time falls somewhere between $1.05\sqrt{D^*/g} < t_b < 1.86\sqrt{D^*/g}$ and is usually a few tenths of a second.

The burn-out time of any thermal element will vary based on the concentration of oxygen in the gas surrounding it[3]. Oxygen is consumed in any given grid cell based on the amount of heat generated in that grid cell. The source term in the oxygen transport equation becomes

$$\dot{W}_{O_2}''' = -\frac{\dot{q}'''}{\Delta H_{O_2}} \tag{33}$$

where ΔH_{O_2} is the amount of heat liberated per unit mass of oxygen consumed (by default 13,100 kJ/kg). When the oxygen mass fraction Y_{O_2} falls to a certain prescribed lower limit, combustion is assumed to stop, and the unburned fuel associated with the thermal elements remains unburned until more oxygen can be found. This combustion model is preliminary. In cases where a fire in a room is spreading to the point of flashover, it can no longer be assumed that there is a constant flux of fuel emanating from the burning surfaces, nor can it be assumed that the fuel even burns. In simulations approaching flashover, this simple model breaks down, and an improved combustion model is being developed.

Another useful input parameter associated with a given solid fuel is the available potential energy per unit volume of the unburned fuel. If prescribed, the computational cell representing a piece of the fuel will disappear once the potential energy has been liberated. This parameter is denoted by $\dot{q}_f'$ or Heat Released Per Unit Volume, and is expressed in units of kJ/m³. If prescribed, this parameter permits fire spread through and consumption of the solid fuel, as in the burning of a boxed commodity or a wood crib.

---

[3]By default, oxygen transport is not included in an LES calculation, and the burn-out time of any thermal element is based on standard flame height correlations.

3.2 One-step, Finite-rate Combustion

In a DNS calculation, the diffusion of fuel and oxygen can be modeled directly, thus it is possible to implement a relatively simple one-step chemical reaction. Consider the reaction of oxygen and a hydrocarbon fuel

$$v_{C_xH_y} C_xH_y + v_{O_2} O_2 \longrightarrow v_{CO_2} CO_2 + v_{H_2O} H_2O \tag{34}$$
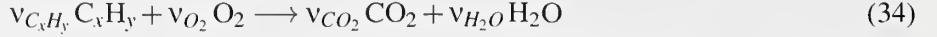
The reaction rate is given by the expression

$$\frac{d[C_xH_y]}{dt} = -B [C_xH_y]^a [O_2]^b e^{-E/RT} \tag{35}$$

Suggested values of B, E, a and b for various hydrocarbon fuels are given in Refs. [15, 16]. It should be understood that the implementation of any of these one-step reaction schemes is still very much a research exercise because it is not universally accepted that combustion phenomena can be represented by such a simple mechanism. Efforts are currently underway to determine in what cases a one-step reaction mechanism provides a valid description of the combustion process.

4 Thermal Boundary Conditions

There are four types of thermal boundary conditions at solid surfaces: adiabatic, fixed temperature, thermally-thin or thermally-thick. The choice of boundary condition depends on the surface material and whether or not it plays a role in the fire. The simplest boundary condition is adiabatic, that is, no heat transfer at all. In this case, the solid is assumed to be at the same temperature as the surrounding gas. The next type of boundary condition is where a temperature is prescribed at the solid surface. If the surface material is assumed to be thermally-thick, the one-dimensional heat conduction equation is applied in the direction n normal to the solid surface

$$\rho_s \, c_s \, \frac{\partial T_s}{\partial t} = k_s \, \frac{\partial^2 T_s}{\partial n^2} \quad ; \quad -k_s \frac{\partial T_s}{\partial n}\bigg|_{n=0} = \dot{q}_c'' + \dot{q}_r'' - \dot{q}_{rr}'' \tag{36}$$

where ρ_s, c_s and k_s are the density, specific heat and conductivity of the material; and $\dot{q}_c''$, $\dot{q}_r''$, $\dot{q}_{rr}''$ are the convective, radiative and re-radiative fluxes at the surface. If the surface material is assumed to be thermally-thin, its temperature is governed by its density, specific heat and thickness δ

$$\frac{dT_s}{dt} = \frac{\dot{q}_c'' + \dot{q}_r'' - \dot{q}_{rr}''}{\rho_s c_s \delta} \tag{37}$$

In this case, the individual values of the parameters ρ_s, c_s and δ are not as important as their product.

The heat fluxes to the surface for either a thermally-thick or thermally-thin material consist of gains and losses from convection and radiation. The convective heat flux to the surface $\dot{q}_c''$ is either obtained directly from the gradient of the gas temperature at the boundary in a DNS calculation

$$\dot{q}_c'' = -k \frac{\partial T}{\partial n} \tag{38}$$

or it is obtained from a correlation of the form

$$\dot{q}_c'' = h \, \Delta T \quad \text{W/m}^2 \quad ; \quad h = C |\Delta T|^{\frac{1}{3}} \quad \text{W/m}^2\text{/K} \tag{39}$$

in an LES calculation. Here ΔT is the difference between the wall and gas temperature, and C is an empirical constant with a default value of 1.43 for a horizontal surface and 0.95 for a vertical surface [17].

9

The radiative heat flux to the surface, $\dot{q}_r''$, is calculated based on the assumption that a prescribed fraction of the heat released from the burning thermal elements is radiated away, and this energy is absorbed by the surrounding surfaces, as well as by the smoke-laden gas. At a given point $\mathbf{x}$ on a solid surface, the radiative flux is given as

$$\dot{q}_r'' = \sum_{i=1}^{N_p} \cos(\phi_i) \frac{\chi_r \dot{q}_{p,i}}{4\pi |\mathbf{x}_{p,i} - \mathbf{x}_s|^2} e^{-\int \kappa(l)\, dl} \tag{40}$$

$\mathbf{x}_{p,i}$ is the position and $\dot{q}_{p,i}$ is the heat release rate of the ith thermal element, dl is an element of the line segment connecting the points $\mathbf{x}_{p,i}$ and $\mathbf{x}_s$, and ϕ_i is the angle formed by the normal to the surface and the vector $\mathbf{x}_{p,i} - \mathbf{x}_s$.

Energy from the heated wall is lost as thermal radiation according to

$$\dot{q}_{rr}'' = \sigma \varepsilon \left(T_s^4 - T_\infty^4 \right) \tag{41}$$

where σ is the Stefan-Boltzmann constant $\sigma = 5.67 \times 10^{-8}$ W/m^2/K^4, and ε is the emissivity of the surface.

5 Sprinklers

Simulating the effects of a sprinkler spray involves a number of pieces: predicting activation, computing the droplet trajectories and tracking the water as it drips onto the burning commodity.

5.1 Sprinkler Activation

The temperature of the sensing element of a given sprinkler is estimated from the differential equation put forth by Heskestad and Bill [18], with the addition of several terms to account for radiative heating and cooling by water droplets in the gas stream from previously activated sprinklers

$$\frac{dT_l}{dt} = \frac{\sqrt{|\mathbf{u}|}}{\text{RTI}}(T_g - T_l) - \frac{C}{\text{RTI}}(T_l - T_m) - \frac{C_2}{\text{RTI}}\beta|\mathbf{u}| \tag{42}$$

Here T_l is the link temperature, T_g is the gas temperature in the neighborhood of the link, T_m is the temperature of the sprinkler mount, and β is the volume fraction of (liquid) water in the gas stream. The sensitivity of the detector is characterized by the value of RTI. The amount of heat conducted away from the link by the mount is indicated by the "C-Factor", C. The constant C_2 has been empirically determined by DiMarzo [19] to be 6×10^6 K/(m/s)$^{\frac{1}{2}}$, and its value is relatively constant for different types of sprinklers.

5.2 Sprinkler Droplet Size Distribution

Once activation is predicted, a sampled set of spherical water droplets is tracked from the sprinkler to either the floor or the burning commodity. In order to compute the droplet trajectories, the initial size and velocity of each droplet must be prescribed. This is done in terms of random distributions. The initial droplet size distribution of the sprinkler spray is expressed in terms of its Cumulative Volume Fraction (CVF), a function that relates the fraction of the water volume (mass) transported by droplets less than a given diameter. Researchers at Factory Mutual have suggested that the CVF for an industrial sprinkler may be represented by a combination of log-normal and Rosin-Rammler distributions [20]

$$F(d) = \begin{cases} \frac{1}{\sqrt{2\pi}} \int_0^d \frac{1}{\sigma d'} e^{-\frac{[\ln(d'/d_m)]^2}{2\sigma^2}} \, dd' & (d \leq d_m) \\ 1 - e^{-0.693\left(\frac{d}{d_m}\right)^{\gamma}} & (d_m < d) \end{cases} \tag{43}$$

where d_m is the median droplet diameter (i.e. half the mass is carried by droplets with diameters of d_m or less), and γ and σ are empirical constants equal to about 2.4 and 0.6, respectively. The median drop diameter is a function of the sprinkler orifice diameter, operating pressure, and geometry. Research at Factory Mutual has yielded a correlation for the median droplet diameter [21]

$$\frac{d_m}{D} \propto \text{We}^{-\frac{1}{3}} \tag{44}$$

where D is the orifice diameter of the sprinkler. The Weber number, the ratio of inertial forces to surface tension forces, is given by

$$\text{We} = \frac{\rho_w U^2 D}{\sigma_w} \tag{45}$$

where ρ_w is the density of water, U is the water discharge velocity, and σ_w is the water surface tension (72.8×10^{-3} N/m at 20°C). The discharge velocity can be computed from the mass flow rate, which is a function of the sprinkler's operating pressure and K-Factor. FM reports that the constant of proportionality in Eq. (44) appears to be independent of flow rate and operating pressure. Three different sprinklers were tested

in their study with orifice diameters of 16.3 mm, 13.5 mm, 12.7 mm and the constants were approximately 4.3, 2.9, 2.3, respectively. The strike plates of the two smaller sprinklers were notched, while that of the largest sprinkler was not [21].

In the numerical algorithm, the size of the sprinkler droplets are chosen to mimic the Rosin-Rammler/log-normal distribution. A Probability Density Function (PDF) for the droplet diameter is defined

$$f(d) = \frac{F'(d)}{d^3} \Big/ \int_0^\infty \frac{F'(d')}{d'^3} \, dd' \tag{46}$$

Droplet diameters are randomly selected by equating the Cumulative Number Fraction of the droplet distribution with a uniformly distributed random variable U

$$U(d) = \int_0^d f(d') \, dd' \tag{47}$$

Figure 1 displays typical Cumulative Volume Fraction and Cumulative Number Fraction functions.
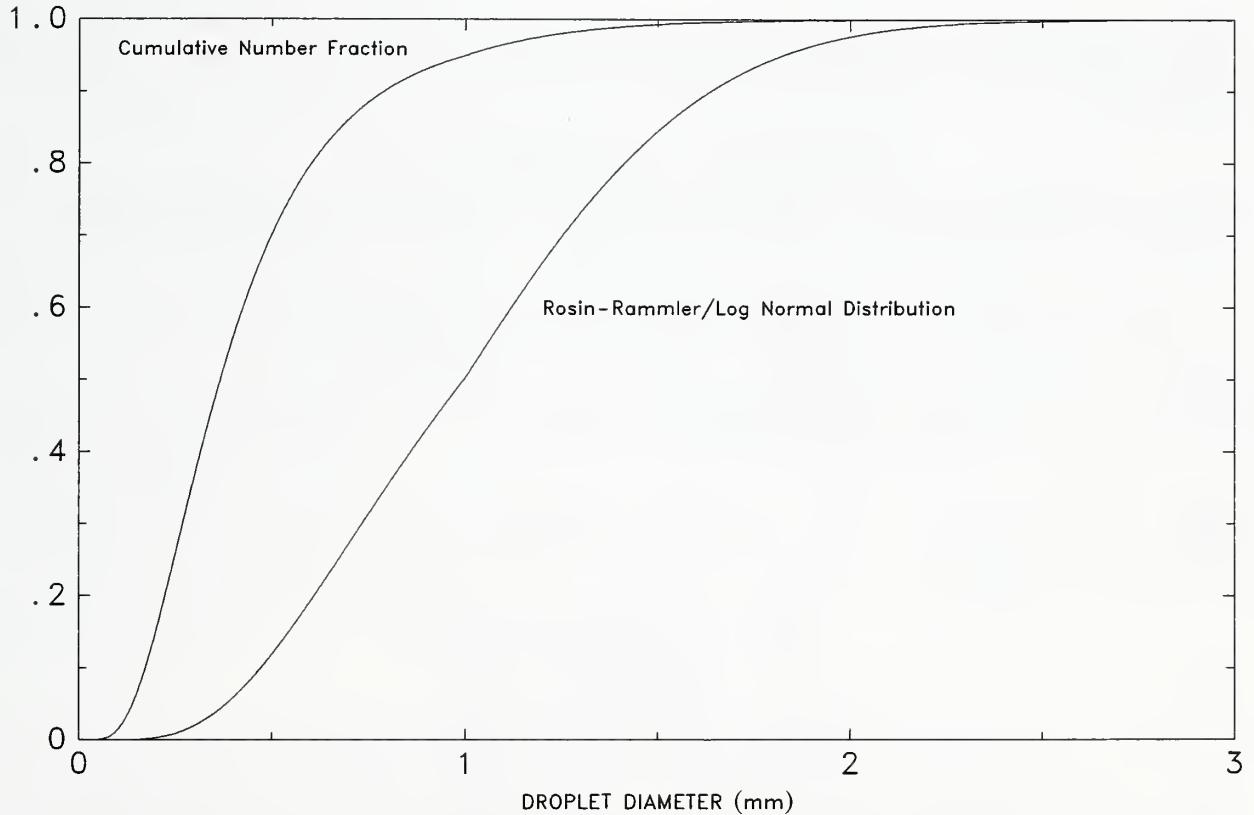
Figure 1: Cumulative Volume Fraction and Cumulative Number Fraction functions of the droplet size distribution from a typical industrial scale sprinkler. The median diameter d_n is 1 mm, $\sigma = 0.6$ and $\gamma = 2.43$.

Every droplet from a given sprinkler is not tracked. Instead, a sampled set of the droplets is tracked. Typically, 1,000 particles per sprinkler per second are tracked. The total number of droplets represented by each computed droplet is given by $\dot{m}_w / (\dot{n} \overline{m_d})$, where $\dot{m}_w$ is the mass flow rate of water from a single sprinkler, $\dot{n}$ is the number of droplets tracked per sprinkler per second, and $\overline{m_d}$ is the average mass of a

droplet. The average mass of a droplet can be expressed in terms of the diameter PDF

$$\overline{m}_d = \int_0^\infty f(d') \frac{4}{3} \pi \rho_w \left(\frac{d'}{2}\right)^3 dd' = \frac{1}{6} \pi \rho_w \int_0^\infty F'(d') \, dd' \bigg/ \int_0^\infty \frac{F'(d')}{d'^3} \, dd' \tag{48}$$

where ρ_w is the density of water. The number of droplets tracked per sprinkler per second, $\dot{n}$, is controlled by the user.

5.3 Sprinkler Droplet Trajectory in Air

For a sprinkler spray, the force term $\mathbf{f}$ in Eq. (3) represents the momentum transferred from the water droplets to the gas. It is obtained by summing the force transferred from each droplet in a grid cell and dividing by the cell volume

$$\mathbf{f} = \frac{1}{2} \frac{\sum \rho C_d \pi r_d^2 (\mathbf{u}_d - \mathbf{u}) |\mathbf{u}_d - \mathbf{u}|}{\delta x \, \delta y \, \delta z} \tag{49}$$

where C_d is a drag coefficient, $\mathbf{u}_d$ is the velocity of the droplet, $\mathbf{u}$ is the velocity of the gas, ρ is the density of the gas, and $\delta x \, \delta y \, \delta z$ is the volume of the grid cell. The trajectory of an individual droplet is governed by the equation

$$\frac{d}{dt}(m_d \mathbf{u}_d) = m_d \mathbf{g} - \frac{1}{2} \rho C_d \pi r_d^2 (\mathbf{u}_d - \mathbf{u}) |\mathbf{u}_d - \mathbf{u}| \tag{50}$$

where m_d is the mass of the droplet. The drag coefficient is a function of the local Reynolds number

$$C_D = \begin{cases} 24/\text{Re} & \text{Re} < 1 \\ 24 \left(1 + 0.15 \text{Re}^{0.687}\right)/\text{Re} & 1 < \text{Re} < 1000 \\ 0.44 & 1000 < \text{Re} \end{cases} \tag{51}$$

$$\text{Re} = \frac{\rho |\mathbf{u}_d - \mathbf{u}| 2 r_d}{\mu} \tag{52}$$

where μ is the dynamic viscosity of air. The sprinkler spray droplet temperature T_d and mass m_d are governed by the following equations

$$\frac{dT_d}{dt} = \frac{A_s h_d (T_g - T_d)}{c_w m_d} \qquad T_d < T_v \tag{53}$$

$$\frac{dm_d}{dt} = -\frac{A_s h_d (T_g - T_d)}{h_v} \qquad T_d = T_v \tag{54}$$

where c_w is the specific heat of water, h_v is the energy of vaporization of water, $A_s = 4\pi r_d^2$ is the surface area of the droplet, T_g is the gas temperature, T_v is the vaporization temperature of water, h_d is the heat transfer coefficient, given by

$$h_d = \frac{\text{Nu} \, k}{2 r_d} \tag{55}$$

Nu is the Nusselt number given by

$$\text{Nu} = 2 + 0.6 \, \text{Re}^{\frac{1}{2}} \, \text{Pr}^{\frac{1}{3}} \tag{56}$$

A good approximation for the Prandtl number is about 0.7, and k is the thermal conductivity of air.

13

5.4 Sprinkler Droplet Transport on a Surface

When a water droplet hits a solid horizontal surface, it is assigned a random horizontal direction and moves at a fixed velocity until it reaches the edge, at which point it drops straight down at the same fixed velocity. This "dripping" velocity has been measured to be on the order of 0.5 m/s [22]. Both the temperature of non-burning surfaces and the heat release rate of burning surfaces are affected by the droplets. At non-burning surfaces, water absorbs heat from the hot surface and radiant energy from the fire. The equations are slightly different than those governing heat transfer to the airborne drops.

$$\frac{dT_d}{dt} = \frac{0.5A_s(h_s(T_s - T_d) + \dot{q}_r'')}{c_w m_d} \qquad T_d < T_v \tag{57}$$

$$\frac{dm_d}{dt} = -\frac{0.5A_s(h_s(T_s - T_d) + \dot{q}_r'')}{h_v} \qquad T_d = T_v \tag{58}$$

where T_s is the temperature of the surface, $\dot{q}_r''$ is the incoming radiant energy flux, and h_s is the heat transfer coefficient between the solid surface and the water droplet, assumed to be constant at 3000 W/m^2/K [22].

5.5 Fire Suppression by Water

The above two sections describe heat transfer from a droplet of water to a hot gas, a hot solid, or both. Although there is some uncertainty in the values of the respective heat transfer coefficients, the fundamental physics are fairly well understood. However, when the water droplets encounter burning surfaces, simple heat transfer correlations become more difficult to apply. The reason for this is that the water is not only cooling the surface and the surrounding gas, but it is also changing the pyrolysis rate of the fuel. If the surface of the fuel is planar, it is possible to characterize the decrease in the pyrolysis rate as a function of the decrease in the total heat feedback to the surface. Unfortunately, most fuels of interest in fire applications are multi-component solids with complex geometry at scales unresolvable by the computational grid.

To date, most of the work in this area has been performed at Factory Mutual. An important paper on the subject is by Yu *et al.* [23]. The authors consider dozens of rack storage commodity fires of different geometries and water application rates, and characterize the suppression rates in terms of a few global parameters. Their analysis yields an expression for the total heat release rate from a rack storage fire after sprinkler activation

$$\dot{Q} = \dot{Q}_0 \, e^{-k(t-t_0)} \tag{59}$$

where $\dot{Q}_0$ is the total heat release rate at the time of application t_0, and k is a fuel-dependent constant. For the FMRC Standard Plastic commodity k is given as

$$k = 0.716 \, \dot{m}_w'' - 0.0131 \quad \text{s}^{-1} \tag{60}$$

where $\dot{m}_w''$ is the flow rate of water impinging on the box tops, divided by the area of exposed surface (top and sides). It is expressed in units of kg/m^2/s. For the Class II commodity, k is given as

$$k = 0.536 \, \dot{m}_w'' - 0.0040 \quad \text{s}^{-1} \tag{61}$$

Unfortunately, this analysis is based on global water flow and burning rates. Equation (59) accounts for both the cooling of non-burning surfaces as well as the decrease in heat release rate of burning surfaces. In the FDS model, the cooling of unburned surfaces and the reduction in the heat release rate are computed locally, thus it is awkward to apply a global suppression rule. However, the exponential nature of suppression by water is observed both locally and globally, thus it is assumed that the local heat release rate of the fuel can be expressed in the form [22]

$$\dot{q}_f''(t) = \dot{q}_{f,0}''(t) \left(e^{-\int k_1 dt} + k_2(t - t_0) \right) \tag{62}$$

14

Here $\dot{q}''_{f,0}(t)$ is the heat release rate per unit area of the fuel when no water is applied and k_1 and k_2 are functions of the local water mass per unit area, m''_w, expressed in units of kg/m^2.

$$k_1 = a_1 m''_w \quad \text{s}^{-1} \tag{63}$$

$$k_2 = a_2 m''_w + b_2 \quad \text{s}^{-1} \tag{64}$$

The linear term in Eq. (62) is based on the observation that for a boxed commodity, it is possible for the local heat release rate to increase as the fire burns into the box and is protected from the water droplets by material overhead, thus often a gradual increase in the heat release rate is observed following the initial decrease after water is applied.

To develop the suppression model for the FMRC Standard Plastic commodity, 19 experiments were conducted at UL under a 2 MW calorimeter [22]. These experiments were designed as small-scale RDD (Required Delivered Density) tests. The fuel/sprinkler arrangement consisted of four boxes of the FMRC Plastic Commodity. The boxes were stacked two high. The two stacks were positioned 15 cm (6 in) apart, the same separation that is commonly used in full-scale tests. A water applicator was positioned above the boxes to deliver a uniform water flux onto the tops of the boxes. The applicator consisted of four nozzles that were 60 cm (2 ft) apart and 30 cm (1 ft) above the plane of the box tops. Several nozzle sizes were used, depending on the desired water flow. Table 4 lists the average water application rate per unit area and the time of water application. The time of water application was varied from 30 s to 200 s. The water flux at the box top was varied from 0.03 kg/m^2/s (0.05 gpm/ft^2) to 0.66 kg/m^2/s (0.97 gpm/ft^2). The ignition source

Table 1: Time and Rate of Water Application

Test No.	Application Time (s)	Total Water Flow (L/s)	Total Water Flow (gpm)	Average Water Flux (L/m²/s)	Average Water Flux (gpm/ft²)
1	380	0.98	15.5	0.66	0.97
2	470	0.57	9.0	0.38	0.56
3	65	0.41	6.5	0.28	0.41
4	106	0.41	6.5	0.28	0.41
5	115	0.11	1.8	0.074	0.11
6	122	0.11	1.8	0.074	0.11
7	150	0.079	1.3	0.053	0.08
8	93	0.11	1.8	0.074	0.11
9	93	0.21	3.3	0.14	0.20
10	110	0.21	3.3	0.14	0.20
11	205	0.21	3.3	0.14	0.20
12	116	0.16	2.5	0.11	0.16
13	63	0.16	2.5	0.11	0.16
14	64	0.28	4.5	0.19	0.28
15	71	0.079	1.3	0.053	0.08
16	62	0.047	0.9	0.032	0.05
17	104	0.047	0.9	0.032	0.05
18	58	0.079	1.3	0.053	0.08
19	30	0.079	1.3	0.053	0.08

was a propane igniter that consisted of two parallel 12.5 mm diameter copper tubes each 30 cm long.

The heat release rate histories for the experiments and the simulations are given in Figs. 2–4. The decay, and in some cases re-growth, of the fire is captured reasonably well by the simulations. A weakness of the

suppression algorithm, however, is its reliance on 5 empirical coefficients that are not easily measured. It is hoped that further work in this area will provide more insight into fire suppression, and the numerical algorithm will reflect this improved understanding.
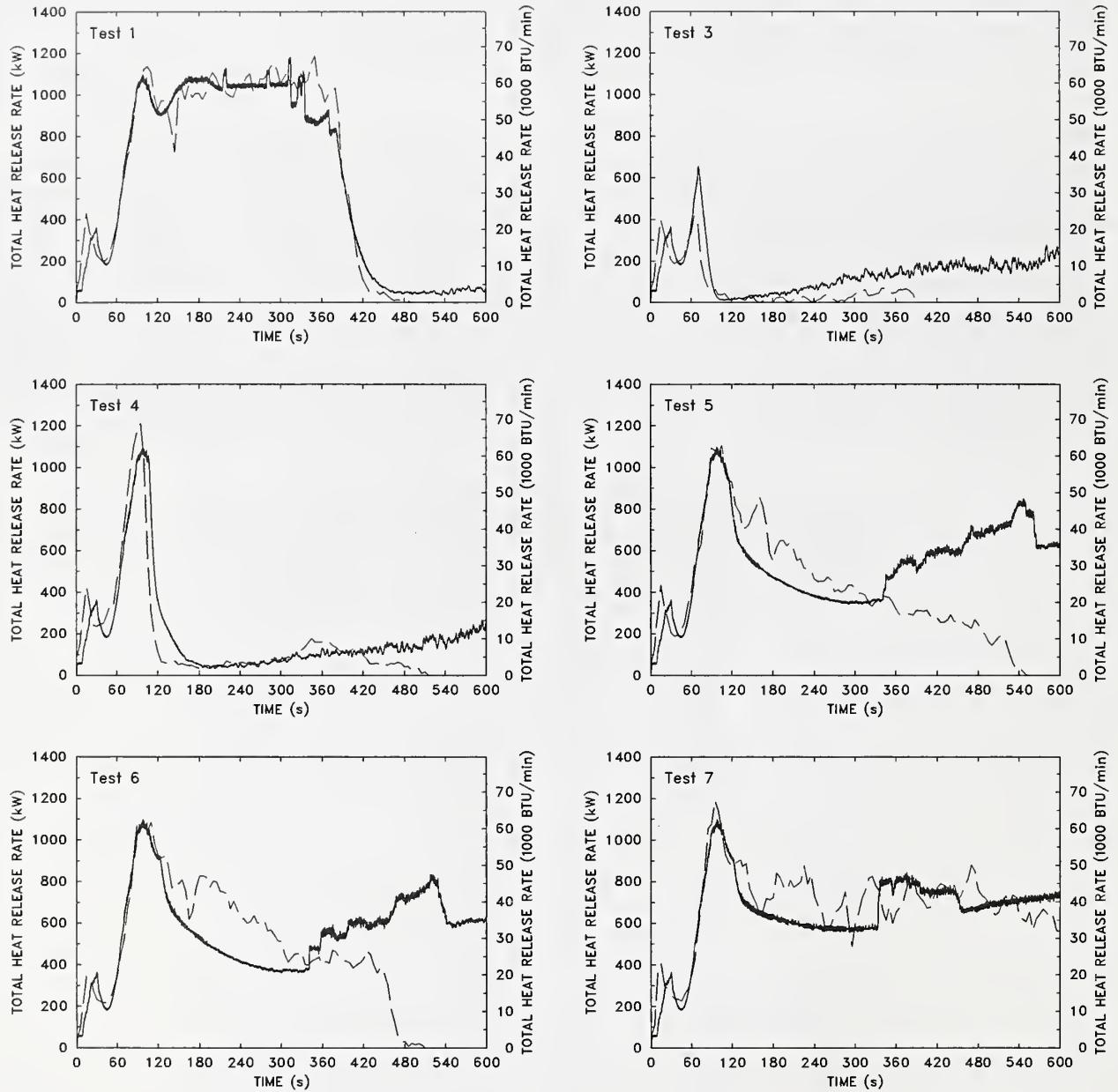
Figure 2: Simulated (solid lines) and experimental (dashed lines) heat release rates for Tests 1, 3–7.
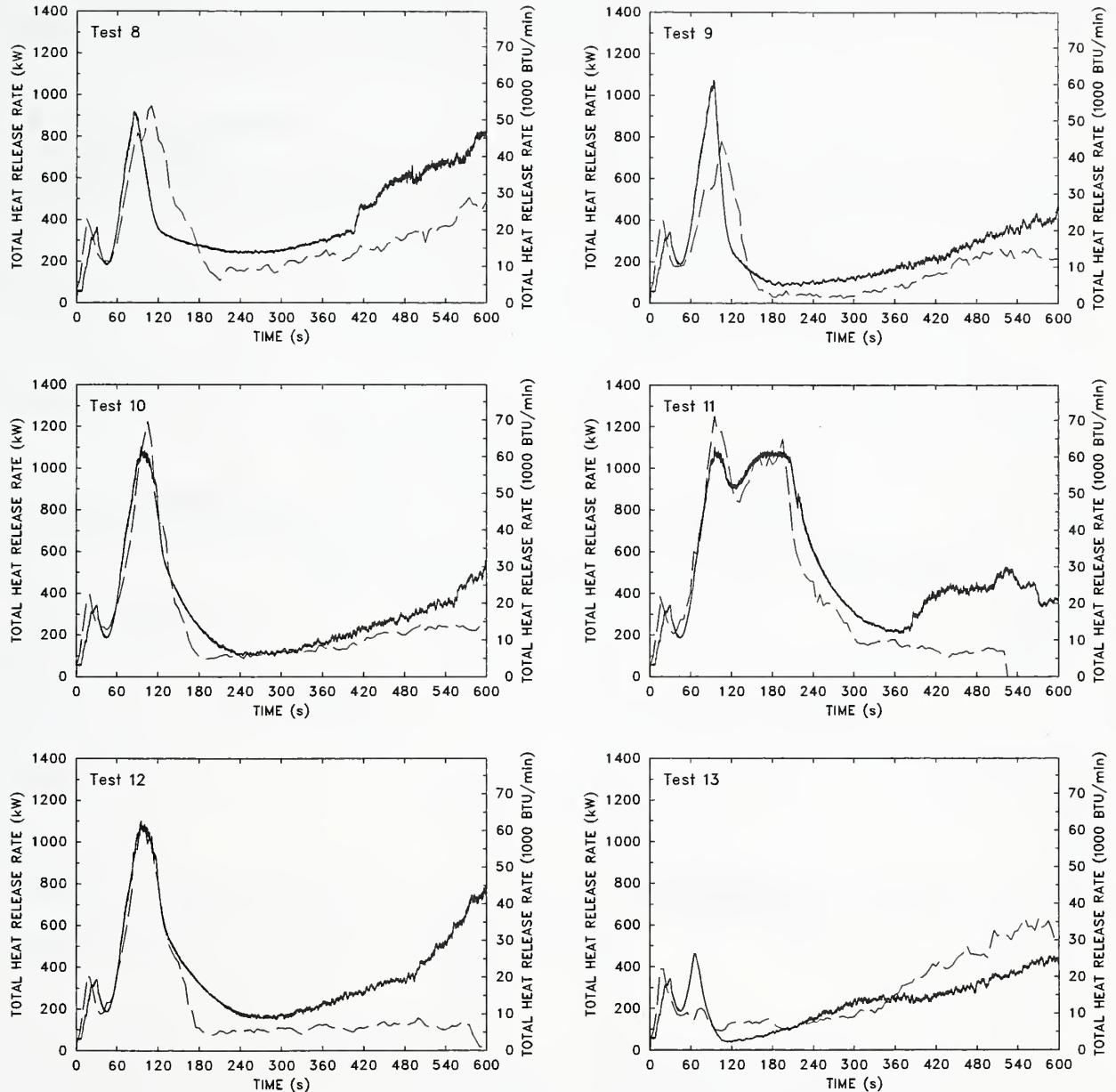
**Figure 3: Simulated (solid lines) and experimental (dashed lines) heat release rates for Tests 8–13.**
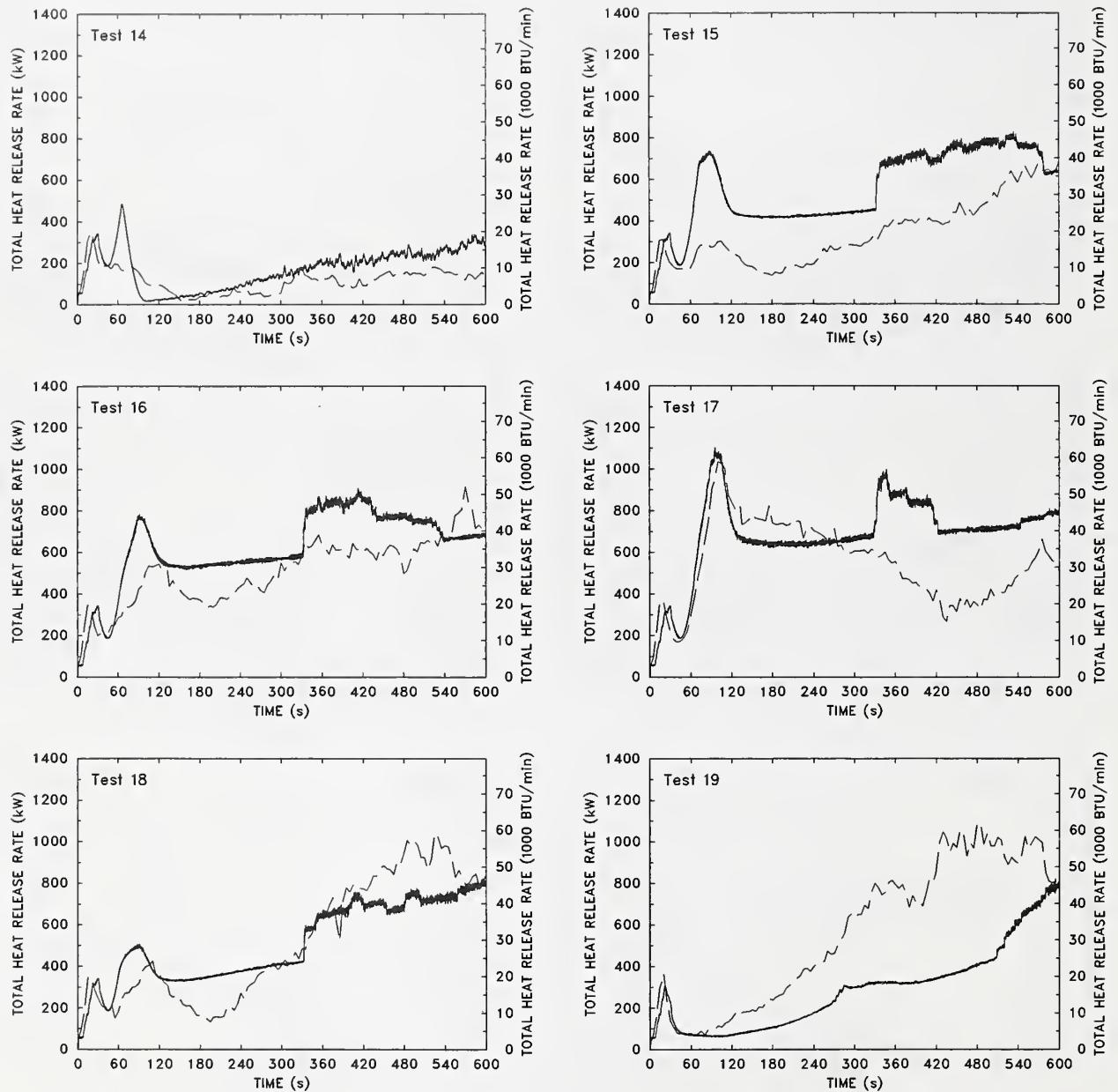
Figure 4: Simulated (solid lines) and experimental (dashed lines) heat release rates for Tests 14–19.

6 Numerical Method

This section presents the details of the numerical algorithm. First the equations that are being solved are presented. Each of the conservation equations emphasize the importance of the velocity divergence and vorticity fields, as well as the close relationship between the thermally expandable fluid equations [5] and the Boussinesq equations for which the authors have developed highly efficient solution procedures [24, 25]. All spatial derivatives are approximated by second order central differences and the flow variables are updated in time using an explicit second order predictor-corrector scheme.

6.1 Simplified Equations

Regardless of whether one is performing an LES or a DNS calculation, the overall solution algorithm is the same. The equations derived in Section 2 that are to be solved numerically are listed again here.

Conservation of Mass

$$\frac{\partial \rho}{\partial t} + \mathbf{u} \cdot \nabla \rho = -\rho \nabla \cdot \mathbf{u} \tag{65}$$

Conservation of Species

$$\frac{\partial \rho Y_l}{\partial t} + \mathbf{u} \cdot \nabla \rho Y_l = -\rho Y_l \nabla \cdot \mathbf{u} + \nabla \cdot \rho D \nabla Y_l + \dot{W}_l''' \tag{66}$$

Conservation of Momentum

$$\frac{\partial \mathbf{u}}{\partial t} + \mathbf{u} \times \omega + \nabla \mathcal{H} = \frac{1}{\rho} \left((\rho - \rho_\infty)\mathbf{g} + \mathbf{f} + \nabla \cdot \tau \right) \tag{67}$$

Divergence Constraint

$$\nabla \cdot \mathbf{u} = \frac{\gamma - 1}{\gamma p_0} \left(\dot{q}''' + \nabla \cdot k \nabla T + \nabla \cdot \sum_l c_{p,l} T \rho D \nabla Y_l - \frac{1}{\gamma - 1} \frac{dp_0}{dt} \right) \tag{68}$$

Equation of State

$$p_0(t) = \rho T \mathcal{R} \sum_l Y_l / M_l \tag{69}$$

Notice that the source terms from the energy conservation equation have been incorporated into the divergence and ultimately are involved in the mass conservation equation. The temperature is found from the density and background pressure via the equation of state.

6.2 Temporal Discretization

All calculations start with ambient initial conditions. At the beginning of each time step, the quantities ρ, Y_i^n, $\mathbf{u}^n$, $\mathcal{H}^n$, and p_0^n are known. All other quantities can be derived from them. Note that the superscript $(n+1)_e$ refers to an estimate of the value of the quantities at the $(n+1)$st time step.

1. The thermodynamic quantities ρ, Y_i, and p_0 are estimated at the next time step with an explicit Euler step. For example, the density is estimated

$$\rho^{(n+1)_e} = \rho^n - \delta t (\mathbf{u}^n \cdot \nabla \rho^n + \rho^n \nabla \cdot \mathbf{u}^n) \tag{70}$$

The divergence $(\nabla \cdot \mathbf{u})^{(n+1)_e}$ is formed from these estimated thermodynamic quantities. The normal velocity components at boundaries that are needed to form the divergence are assumed known.

2. A Poisson equation for the pressure is solved with a direct solver

$$\nabla^2 \mathcal{H}^n = -\frac{(\nabla \cdot \mathbf{u})^{(n+1)_e} - (\nabla \cdot \mathbf{u})^n}{\delta t} - \nabla \cdot \mathbf{F}^n \tag{71}$$

Note that the vector $\mathbf{F}$ contains the convective, diffusive and force terms of the momentum equation. These will be described in detail below. Then the velocity is estimated at the next time step

$$\mathbf{u}^{(n+1)_e} = \mathbf{u}^n - \delta t \left(\mathbf{F}^n + \nabla \mathcal{H}^n \right) \tag{72}$$

Note that the divergence of the estimated velocity field is identically equal to the estimated divergence $(\nabla \cdot \mathbf{u})^{(n+1)_e}$ that was derived from the estimated thermodynamic quantities. The time step is checked at this point to ensure that

$$\delta t < \min \left(\frac{\delta x}{u}, \frac{\delta y}{v}, \frac{\delta z}{w} \right) \tag{73}$$

If the time step is too large, it is reduced so that it satisfies the CFL condition and the procedure starts from the beginning of the time step. If the time step satisfies the stability condition, the procedure continues.

3. The thermodynamic quantities ρ, Y_i, and p_0 are corrected at the next time step. For example, the density is corrected

$$\rho^{n+1} = \frac{1}{2} \left(\rho^n + \rho^{(n+1)_e} - \delta t (\mathbf{u}^{(n+1)_e} \cdot \nabla \rho^{(n+1)_e} + \rho^{(n+1)_e} \nabla \cdot \mathbf{u}^{(n+1)_e}) \right) \tag{74}$$

The divergence $(\nabla \cdot \mathbf{u})^{(n+1)}$ is derived from the corrected thermodynamic quantities.

4. The pressure is recomputed using estimated quantities

$$\nabla^2 \mathcal{H}^{(n+1)_e} = -\frac{2(\nabla \cdot \mathbf{u})^{n+1} - (\nabla \cdot \mathbf{u})^{(n+1)_e} - (\nabla \cdot \mathbf{u})^n}{\delta t} - \nabla \cdot \mathbf{F}^{(n+1)_e} \tag{75}$$

The velocity is then corrected

$$\mathbf{u}^{n+1} = \frac{1}{2} \left[\mathbf{u}^n + \mathbf{u}^{(n+1)_e} - \delta t \left(\mathbf{F}^{(n+1)_e} + \nabla \mathcal{H}^{(n+1)_e} \right) \right] \tag{76}$$

Note again that the divergence of the corrected velocity field is identically equal to the corrected divergence.

6.3 Spatial Discretization

Spatial derivatives in the governing equations are written as second order accurate finite differences on a rectilinear grid. The overall domain is a rectangular box that is divided into rectangular grid cells. Each cell is assigned indices i, j and k representing the position of the cell in the x, y and z directions, respectively. Scalar quantities are assigned in the center of each grid cell, thus ρ^n_{ijk} is the density at the nth time step in the center of the cell whose indices are i, j and k. Vector quantities like velocity are assigned at cell faces, thus the x component of velocity u is defined at the faces whose normals are parallel to the x-axis, the y component v is defined at the faces whose normals are parallel to the y-axis, and the z component w is defined at the faces whose normals are parallel to the z-axis. The quantity u^n_{ijk} is the x component of velocity at the forward pointing face of the ijkth cell; $u^n_{i-1,jk}$ is at the backward pointing face of the ijkth cell.

21

6.4 Large Eddy vs. Direct Numerical Simulation

The major difference between an LES and a DNS calculation is the form of the viscosity, and the thermal and material diffusivities. For a Large Eddy Simulation, the dynamic viscosity is defined at cell centers

$$\mu_{ijk} = \rho_{ijk} \left(C_s \Delta\right)^2 |S| \tag{77}$$

where C_s is an empirical constant, $\Delta = \left(\delta x\, \delta y\, \delta z\right)^{\frac{1}{3}}$, and

$$|S|^2 = 2\left(\frac{\partial u}{\partial x}\right)^2 + 2\left(\frac{\partial v}{\partial y}\right)^2 + 2\left(\frac{\partial w}{\partial z}\right)^2 + \left(\frac{\partial u}{\partial y} + \frac{\partial v}{\partial x}\right)^2 + \left(\frac{\partial u}{\partial z} + \frac{\partial w}{\partial x}\right)^2 + \left(\frac{\partial v}{\partial z} + \frac{\partial w}{\partial y}\right)^2 \tag{78}$$

The quantity $|S|$ consists of second order spatial differences averaged at cell centers. The thermal conductivity and material diffusivity of the fluid are related to the viscosity by

$$k_{ijk} = \frac{c_{p,0}\mu_{ijk}}{\mathrm{Pr}} \quad ; \quad (\rho D)_{ijk} = \frac{\mu_{ijk}}{\mathrm{Sc}} \tag{79}$$

where Pr is the Prandtl number and Sc is the Schmidt number, both assumed constant. Note that the specific heat $c_{p,0}$ is that of the dominant species of the mixture. Based on simulations of smoke plumes, C_s is 0.14, Pr and Sc are 0.2. There is no rigorous justification for these choices.

The dynamic viscosity, thermal conductivity and diffusion coefficients for a DNS calculation are defined at cell centers

$$\mu_{ijk} = \sum_l Y_{l,ijk}\, \mu_l(T_{ijk}) \tag{80}$$

$$k_{ijk} = \sum_l Y_{l,ijk}\, k_l(T_{ijk}) \tag{81}$$

$$D_{l,ijk} = D_{l0}(T_{ijk}) \tag{82}$$

where the values for each individual species are approximated from kinetic theory [12]. The term D_{l0} is the binary diffusion coefficient for species l diffusing into the predominant species 0, usually nitrogen. It is often the case that the numerical grid is too coarse to resolve steep gradients in flow quantities when the temperature is near ambient. However, as the temperature increases and the diffusion coefficients increase in value, the situation improves. As a consequence, there is a provision in the numerical algorithm to place a lower bound on the viscous coefficients to avoid numerical instabilities at temperatures close to ambient.

6.5 The Mass Transport Equations

Due to the low Mach number approximation being used in the model, the mass and energy equations are combined by way of the divergence. The divergence of the flow field contains much of the fire-specific source terms described above.

6.5.1 Convective and Diffusive Transport

The density at the center of the ijkth cell is updated in time with the following predictor-corrector scheme. In the predictor step, the density at the $(n+1)$st time level is estimated based on information at the nth level

$$\frac{\rho_{ijk}^{(n+1)_e} - \rho_{ijk}^n}{\delta t} + (\mathbf{u}\cdot\nabla\rho)_{ijk}^n = -\rho_{ijk}^n(\nabla\cdot\mathbf{u})_{ijk}^n \tag{83}$$

Following the prediction of the velocity and background pressure at the $(n+1)$st time level, the density is corrected

$$\frac{\rho_{ijk}^{(n+1)} - \frac{1}{2}\left(\rho_{ijk}^n + \rho_{ijk}^{(n+1)_e}\right)}{\frac{1}{2}\delta t} + (\mathbf{u}\cdot\nabla\rho)_{ijk}^{(n+1)_e} = -\rho_{ijk}^{(n+1)_e}(\nabla\cdot\mathbf{u})_{ijk}^{(n+1)_e} \tag{84}$$

The species conservation equations are differenced the same way

$$\frac{(\rho Y_l)_{ijk}^{(n+1)_e} - (\rho Y_l)_{ijk}^n}{\delta t} + (\mathbf{u}\cdot\nabla\rho Y_l)_{ijk}^n = -(\rho Y_l)_{ijk}^n(\nabla\cdot\mathbf{u})_{ijk}^n + (\nabla\cdot\rho D\nabla Y_l)_{ijk}^n + \dot{W}_{ijk}''' \tag{85}$$

at the predictor step, and

$$\frac{(\rho Y_l)_{ijk}^{(n+1)} - \frac{1}{2}\left((\rho Y_l)_{ijk}^n + (\rho Y_l)_{ijk}^{(n+1)_e}\right)}{\frac{1}{2}\delta t} + (\mathbf{u}\cdot\nabla\rho Y_l)_{ijk}^{(n+1)_e} = -(\rho Y_l)_{ijk}^{(n+1)_e}(\nabla\cdot\mathbf{u})_{ijk}^{(n+1)_e} + (\nabla\cdot\rho D\nabla Y_l)_{ijk}^{(n+1)_e} + \dot{W}_{ijk}''' \tag{86}$$

at the corrector step.

The convective terms are written as upwind-biased differences in the predictor step and downwind-biased differences in the corrector step. In the expressions to follow, the symbol $\pm$ means $+$ in the predictor step and $-$ in the corrector step. The opposite is true for $\mp$.

$$(\mathbf{u}\cdot\nabla\rho)_{ijk} = \frac{1\mp\varepsilon_u}{2}u_{ijk}\frac{\rho_{i+1,jk} - \rho_{ijk}}{\delta x} + \frac{1\pm\varepsilon_u}{2}u_{i-1,jk}\frac{\rho_{ijk} - \rho_{i-1,jk}}{\delta x} +$$
$$\frac{1\mp\varepsilon_v}{2}v_{ijk}\frac{\rho_{i,j+1,k} - \rho_{ijk}}{\delta y} + \frac{1\pm\varepsilon_v}{2}v_{i,j-1,k}\frac{\rho_{ijk} - \rho_{i,j-1,k}}{\delta y} +$$
$$\frac{1\mp\varepsilon_w}{2}w_{ijk}\frac{\rho_{ij,k+1} - \rho_{ijk}}{\delta z} + \frac{1\pm\varepsilon_w}{2}w_{ij,k-1}\frac{\rho_{ijk} - \rho_{ij,k-1}}{\delta z} \tag{87}$$

$$(\mathbf{u}\cdot\nabla\rho Y_l)_{ijk} = \frac{1\mp\varepsilon_u}{2}u_{ijk}\frac{(\rho Y_l)_{i+1,jk} - (\rho Y_l)_{ijk}}{\delta x} + \frac{1\pm\varepsilon_u}{2}u_{i-1,jk}\frac{(\rho Y_l)_{ijk} - (\rho Y_l)_{i-1,jk}}{\delta x} +$$
$$\frac{1\mp\varepsilon_v}{2}v_{ijk}\frac{(\rho Y_l)_{i,j+1,k} - (\rho Y_l)_{ijk}}{\delta y} + \frac{1\pm\varepsilon_v}{2}v_{i,j-1,k}\frac{(\rho Y_l)_{ijk} - (\rho Y_l)_{i,j-1,k}}{\delta y} +$$
$$\frac{1\mp\varepsilon_w}{2}w_{ijk}\frac{(\rho Y_l)_{ij,k+1} - (\rho Y_l)_{ijk}}{\delta z} + \frac{1\pm\varepsilon_w}{2}w_{ij,k-1}\frac{(\rho Y_l)_{ijk} - (\rho Y_l)_{ij,k-1}}{\delta z} \tag{88}$$

Note that without the inclusion of the ε's, these are simple central difference approximations. The ε's are local CFL numbers, $\varepsilon_u = u\delta t/\delta x$, $\varepsilon_v = v\delta t/\delta y$, and $\varepsilon_w = w\delta t/\delta z$, where the velocity components are those

that immediately follow. Their role is to bias the differencing upwind. Where the local CFL number is near unity, the difference becomes nearly fully upwinded. Where the local CFL number is much less than unity, the differencing is more centralized [26].

The divergence in both the predictor and corrector step is discretized

$$(\nabla \cdot \mathbf{u})_{ijk} = \frac{\gamma - 1}{\gamma p_0} \left(\dot{q}'''_{ijk} + (\nabla \cdot k \nabla T)_{ijk} + \sum_l (\nabla \cdot T c_{p,l} \rho D \nabla Y_l)_{ijk} - \frac{1}{\gamma - 1} \left(\frac{dp_0}{dt} \right) \right) \tag{89}$$

The thermal and material diffusion terms are pure central differences, with no upwind or downwind bias, thus they are differenced the same way in both the predictor and corrector steps

$$(\nabla \cdot k \nabla T)_{ijk} = \frac{1}{\delta x} \left[k_{i+\frac{1}{2},jk} \frac{T_{i+1,jk} - T_{ijk}}{\delta x} - k_{i-\frac{1}{2},jk} \frac{T_{ijk} - T_{i-1,jk}}{\delta x} \right] +$$
$$\frac{1}{\delta y} \left[k_{i,j+\frac{1}{2},k} \frac{T_{i,j+1,k} - T_{ijk}}{\delta y} - k_{i,j-\frac{1}{2},k} \frac{T_{ijk} - T_{i,j-1,k}}{\delta y} \right] +$$
$$\frac{1}{\delta z} \left[k_{ij,k+\frac{1}{2}} \frac{T_{ij,k+1} - T_{ijk}}{\delta z} - k_{ij,k-\frac{1}{2}} \frac{T_{ijk} - T_{ij,k-1}}{\delta z} \right] \tag{90}$$

$$(\nabla \cdot c_{p,l} T \rho D \nabla Y_l)_{ijk} = \frac{c_{p,l}}{\delta x} \left[T_{i+\frac{1}{2},jk} \, \rho D_{l,i+\frac{1}{2},jk} \frac{Y_{l,i+1,jk} - Y_{l,ijk}}{\delta x} - T_{i-\frac{1}{2},jk} \, \rho D_{l,i-\frac{1}{2},jk} \frac{Y_{l,ijk} - Y_{l,i-1,jk}}{\delta x} \right] +$$
$$\frac{c_{p,l}}{\delta y} \left[T_{i,j+\frac{1}{2},k} \, \rho D_{l,i,j+\frac{1}{2},k} \frac{Y_{l,i,j+1,k} - Y_{l,ijk}}{\delta y} - T_{i,j-\frac{1}{2},k} \, \rho D_{l,i,j-\frac{1}{2},k} \frac{Y_{l,ijk} - Y_{l,i,j-1,k}}{\delta y} \right] +$$
$$\frac{c_{p,l}}{\delta z} \left[T_{ij,k+\frac{1}{2}} \, \rho D_{l,ij,k+\frac{1}{2}} \frac{Y_{l,ij,k+1} - Y_{l,ijk}}{\delta z} - T_{ij,k-\frac{1}{2}} \, \rho D_{l,ij,k-\frac{1}{2}} \frac{Y_{l,ijk} - Y_{l,ij,k-1}}{\delta z} \right] \tag{91}$$

$$(\nabla \cdot \rho D \nabla Y_l)_{ijk} = \frac{1}{\delta x} \left[\rho D_{l,i+\frac{1}{2},jk} \frac{Y_{l,i+1,jk} - Y_{l,ijk}}{\delta x} - \rho D_{l,i-\frac{1}{2},jk} \frac{Y_{l,ijk} - Y_{l,i-1,jk}}{\delta x} \right] +$$
$$\frac{1}{\delta y} \left[\rho D_{l,i,j+\frac{1}{2},k} \frac{Y_{l,i,j+1,k} - Y_{l,ijk}}{\delta y} - \rho D_{l,i,j-\frac{1}{2},k} \frac{Y_{l,ijk} - Y_{l,i,j-1,k}}{\delta y} \right] +$$
$$\frac{1}{\delta z} \left[\rho D_{l,ij,k+\frac{1}{2}} \frac{Y_{l,ij,k+1} - Y_{l,ijk}}{\delta z} - \rho D_{l,ij,k-\frac{1}{2}} \frac{Y_{l,ijk} - Y_{l,ij,k-1}}{\delta z} \right] \tag{92}$$

The temperature is extracted from the density via the equation of state

$$T_{ijk} = \frac{p_0}{\rho_{ijk} \mathcal{R} \, \Sigma_{l=0}^{N} (Y_{l,ijk}/M_l)} \tag{93}$$

Because only species 1 through N are explicitly computed, the summation is rewritten

$$\sum_{l=0}^{N} \frac{Y_{l,ijk}}{M_l} = \frac{1}{M_0} + \sum_{l=1}^{N} \left(\frac{1}{M_l} - \frac{1}{M_0} \right) Y_l \tag{94}$$

In isothermal calculations involving multiple species, the density can be extracted from the average molecular weight

$$\rho_{ijk} = \frac{p_0}{T_\infty \mathcal{R} \, \Sigma_{l=0}^{N} Y_{l,ijk}/M_l} \tag{95}$$

Again, because only species 1 through N are explicitly computed, this expression can be written

$$\rho_{ijk} = \frac{M_0 p_0}{T_\infty \mathcal{R}} + \sum_{l=1}^{N} \left(1 - \frac{M_0}{M_l} \right) (\rho Y_l)_{ijk} \tag{96}$$

24

6.5.2 Heat Release Rate (LES)

For an LES calculation, heat is added to the flow domain through the use of heat releasing Lagrangian particles, or thermal elements. The thermal elements are ejected from burning surfaces with a normal velocity that is either specified by the user or automatically determined based on the specified heat release rate per unit area, the heat of combustion, and the density of the fuel gases

$$u_n = \frac{\dot{q}_r''}{\Delta H \rho_f} \tag{97}$$

The thermal elements release energy at a constant rate. A specified fraction of the energy is emitted as thermal radiation, and this energy can be re-absorbed by the smoke-laden gases or by the walls if desired. The non-radiated energy from the thermal elements is interpolated on the computational grid. As input, the user specifies the fraction of that energy lost as thermal radiation, χ, and the burn-out time of the elements t_b. The heat release rate per unit volume of the ijkth grid cell is given by the non-radiated energy

$$\dot{q}_{ijk}''' = \frac{\sum_m (1 - \chi_r) \, \dot{q}_{p,m}}{\delta x \, \delta y \, \delta z} \quad ; \quad \dot{q}_{p,m} = \frac{\dot{q}_f''}{t_b \, \dot{n}''} \tag{98}$$

where $\dot{q}_f''$ is the heat release rate per unit area assigned to the surface from which the mth element originated, $\dot{n}''$ is the number of thermal elements introduced per unit time per unit area at this same surface, and the summation is over all thermal elements within the grid cell whose indices are ijk.

If desired, the radiated fraction of the energy from the thermal elements can be re-absorbed by the smoke-laden gases, in which case an additional contribution to the heat release rate per unit volume in a given grid cell is given by

$$\dot{q}_{ijk}''' = \kappa_{ijk} \sum_{m=1}^{N_p} \frac{\chi_r \, \dot{q}_{p,m}}{4\pi |\mathbf{x}_{p,m} - \mathbf{x}_{ijk}|^2} \, e^{-\int \kappa(l) \, dl} \tag{99}$$

Note that here the summation is carried out over all (or a sampling) of the thermal elements, not just those within the ijkth cell. The absorption coefficient κ is computed at the center of the grid cell. It is based on the mass of particulate matter and the temperature within that cell

$$\kappa_{ijk} = 1186 \, T_{ijk} \, f_v \tag{100}$$

Here f_v is the soot volume fraction, given by

$$f_v = \frac{\sum m_{p,m}}{\rho_{soot} \, \delta x \, \delta y \, \delta z} \tag{101}$$

where ρ_{soot} is the density of the soot, and $m_{p,m}$ is the particulate mass carried by the mth thermal element

$$m_{p,m} = \frac{\chi_s \, \dot{q}_{p,m} \, t_b}{\Delta H} \max\left(\frac{t - t_{0,m}}{t_b}, 1\right) \tag{102}$$

Here χ_s is the soot yield of the given fuel, and $t_{0,m}$ is the time when the mth thermal element was introduced at the burning surface.

If sprinklers are flowing, the water droplets can cool the hot gases. The heat release rate per unit volume is decreased

$$\dot{q}_{ijk}''' = -\frac{\sum A_d h_d (T_{ijk} - T_d)}{\delta x \, \delta y \, \delta z} \tag{103}$$

where the summation is carried out over all sprinkler droplets in a grid cell of volume $\delta x \, \delta y \, \delta z$. Here T is the gas temperature, T_d is the droplet temperature, $A_d = 4\pi r_d^2$ is the surface area of a droplet and $h_d = \mathrm{Nu}\, k / 2r_d$ is a heat transfer coefficient.

6.5.3 Heat Release Rate (DNS)

In a DNS calculation, a one-step, finite-rate reaction of a hydrocarbon fuel is assumed

$$\nu_{C_xH_y}\, C_xH_y + \nu_{O_2}\, O_2 \longrightarrow \nu_{CO_2}\, CO_2 + \nu_{H_2O}\, H_2O \tag{104}$$
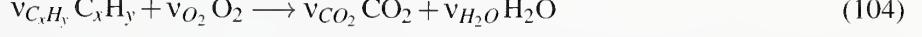
For each grid cell, at the start of a time step where $t = t^n$ and $Y^n_{C_xH_y,ijk} \equiv Y_F(t^n)$ and $Y^n_{O_2,ijk} \equiv Y_O(t^n)$, the following ODE is solved numerically with a 2nd order Runge-Kutta scheme

$$\frac{dY_F}{dt} = -\frac{B\rho^{a+b-1}_{ijk}}{M^b_O M^{a-1}_F} Y_F(t)^a Y_O(t)^b\, e^{-E/RT_{ijk}} \tag{105}$$

$$\frac{dY_O}{dt} = -\frac{\nu_O M_O}{\nu_F M_F} \frac{dY_F}{dt} \tag{106}$$

The temperature T_{ijk} and density ρ_{ijk} are fixed at their values at time t^n and the ODE is iterated from t^n to t^{n+1} in about 100 time steps. The pre-exponential factor B, the activation energy E, and the exponents a and b are input parameters. The average heat release rate over the entire time step is given by

$$\dot{q}'''^n_{ijk} = \Delta H\, \rho^n_{ijk} \frac{Y_F(t^n) - Y_F(t^{n+1})}{\delta t} \tag{107}$$

where $\delta t = t^{n+1} - t^n$. The species mass fractions are adjusted at this point in the calculation (before the convection and diffusion update)

$$Y^n_{l,ijk} = Y_l(t^n) - \frac{\nu_l M_l}{\nu_F M_F} (Y_F(t^n) - Y_F(t^{n+1})) \tag{108}$$

6.5.4 Thermal Boundary Conditions

Four types of thermal boundary conditions are applied at solid surfaces. The first, and simplest, is an adiabatic boundary condition that states that there is no temperature gradient normal to the surface. It is implemented by assigning to the grid cell that is embedded in the solid (the ghost cell) the same temperature as the first cell in the gas (the gas cell).

The second type of boundary condition is where the solid surface has a prescribed temperature (usually this prescribed temperature is a function of time).

The third type of boundary condition assumes the solid to be thermally-thin. The surface temperature is updated in time according to

$$T^{n+1}_w = T^n_w + \delta t_s \frac{\dot{q}''_c + \dot{q}''_r - \dot{q}''_{rr}}{\rho_s c_s \delta} \tag{109}$$

where T_w is the wall temperature, δt_s is the time step used when updating the thermal boundary conditions (usually greater than the hydrodynamic time step δt), and ρ_s, c_s, δ are the input density, specific heat and thickness of the wall. In a DNS calculation where the boundary layer is resolved, the convective flux to the wall is given by

$$\dot{q}''_c = -k \frac{T_{gas} - T_w}{\delta n/2} \tag{110}$$

where δn is the size of a grid cell in the normal direction to the wall. In an LES calculation where the boundary layer is not resolved,

$$\dot{q}''_c = C|T_{gas} - T_w|^{\frac{1}{3}} (T_{gas} - T_w) \quad \text{W/m}^2 \tag{111}$$

where C is an empirical coefficient (0.95 for vertical surface; 1.43 for horizontal), and T_{gas} is the temperature of the gas in the cell bordering the wall. The radiative flux to the wall is given by

$$\dot{q}_r'' = \sum_{m=1}^{N_p} \frac{\chi_r \dot{q}_{p,m} \cos \phi_m}{4\pi |\mathbf{x}_{p,m} - \mathbf{x}|} e^{-\int \kappa(l)\,dl} \qquad (112)$$

where $\dot{q}_{p,m}$ is the heat release rate of the mth thermal element and ϕ_n is the angle formed by the normal to the surface and the line connecting the thermal element and the point on the wall.

The fourth type of thermal boundary condition is for a thermally-thick solid. In this case, a one dimensional heat transfer calculation is performed at each boundary cell designated as thermally-thick. The width of the solid δ is partitioned into N cells, clustered near the front face. The cell boundaries are located at points x_i

$$x_i = f(\xi_i) = s\xi_i + \frac{1-s}{\delta^2}\xi_i^3 \qquad (113)$$

where $0 \le i \le N$, $\xi_i = i\delta\xi$, $\delta\xi = \delta/N$, and $0 < s \le 1$ is a measure of the degree of clustering of the cells at the front face. The width of each cell is $\delta x_i = f'(\xi_{i-\frac{1}{2}})\delta\xi$, $1 \le i \le N$ where $\xi_{i-\frac{1}{2}} = (i - \frac{1}{2})\delta\xi$. The temperature at the center of the ith cell is denoted $T_{s,i}$. These temperatures are updated in time using an implicit Crank-Nicholson scheme

$$\frac{T_{s,i}^{n+1} - T_{s,i}^n}{\delta t} = \frac{\alpha}{2\delta x_i} \left(\frac{T_{s,i+1}^n - T_{s,i}^n}{\delta x_{s,i+\frac{1}{2}}} - \frac{T_{s,i}^n - T_{s,i-1}^n}{\delta x_{s,i-\frac{1}{2}}} + \frac{T_{s,i+1}^{n+1} - T_{s,i}^{n+1}}{\delta x_{i+\frac{1}{2}}} - \frac{T_{s,i}^{n+1} - T_{s,i-1}^{n+1}}{\delta x_{i-\frac{1}{2}}} + \right) \qquad (114)$$

for $1 \le i \le N$. The boundary condition is discretized

$$-k_s \frac{T_{s,1}^{n+1} - T_{s,0}^{n+1}}{\delta x_{\frac{1}{2}}} = \dot{q}_c'' + \dot{q}_r'' - \varepsilon\sigma \left[T_{s,\frac{1}{2}}^{n4} - T_\infty^4 + 4T_{s,\frac{1}{2}}^{n3} \left(T_{s,\frac{1}{2}}^{n+1} - T_{s,\frac{1}{2}}^n \right) \right] \qquad (115)$$

where $T_{s,\frac{1}{2}} = (T_{s,1} + T_{s,0})/2$ is the temperature at the front face. Notice that the radiative emission term has been linearized

$$\varepsilon\sigma \left[T_{s,\frac{1}{2}}^{(n+1)4} - T_\infty^4 \right] \approx \varepsilon\sigma \left[T_{s,\frac{1}{2}}^{n4} - T_\infty^4 + 4T_{s,\frac{1}{2}}^{n3} \left(T_{s,\frac{1}{2}}^{n+1} - T_{s,\frac{1}{2}}^n \right) \right] \qquad (116)$$

The wall temperature is defined $T_w \equiv T_{s,\frac{1}{2}} = (T_{s,0} + T_{s,1})/2$.

Regardless of how the wall temperature is determined, there are two ways of coupling the wall temperature with the fluid calculation. Gas phase temperatures are defined at cell centers; the wall is defined at the boundary of the bordering gas phase cell and a "ghost" cell inside the wall. As far as the gas phase calculation is concerned, the normal temperature gradient at the wall is expressed in terms of the temperature difference between the "gas" cell and the "ghost" cell. The wall temperature affects the gas phase calculation through the prescription of the ghost cell temperature. This ghost cell temperature has no physical meaning on its own. Only the difference between ghost and gas cell temperatures matters, for this defines the heat transfer to the wall. In a DNS calculation, the wall temperature is assumed to be an average of the ghost cell temperature and the temperature of the first cell in the gas, thus the ghost cell temperature is defined

$$T_{ghost} = 2T_w - T_{gas} \qquad (117)$$

For an LES calculation, the heat lost to the boundary is equated with an empirical expression

$$k\frac{T_{gas} - T_{ghost}}{\delta n} = C|T_{gas} - T_w|^{\frac{1}{3}}(T_{gas} - T_w) \qquad (118)$$

where δn is the distance between the center of the ghost cell and the center of the gas cell. This equation is solved for T_{ghost}, so that when the conservation equations are updated, the amount of heat lost to the wall is equivalent to the empirical expression on the right hand side. Note that T_{ghost} is purely a numerical construct. It does not represent the temperature within the wall, but rather establishes a temperature gradient at the wall consistent with the empirical correlation.

27

6.5.5 Species Boundary Conditions

At solid walls there is no transfer of mass, thus the boundary condition for the lth species at a wall is simply

$$Y_{l,ghost} = Y_{l,gas} \tag{119}$$

where the subscripts "ghost" and "gas" are the same as above since the mass fraction, like temperature, is defined at cell centers. At forced flow boundaries either the mass fraction $Y_{,w}$ or the mass flux $\dot{m}''_l$ of species l may be prescribed. Then the ghost cell mass fraction can be derived because, as with temperature, the normal gradient of mass fraction is needed in the gas phase calculation. For cases where the mass fraction is prescribed

$$Y_{l,ghost} = 2Y_{l,w} - Y_{l,gas} \tag{120}$$

For cases where the mass flux is prescribed, the following equation must be solved iteratively

$$\dot{m}''_l = u_n \frac{\rho_{ghost}Y_{l,ghost} + \rho_{gas}Y_{l,gas}}{2} - \rho D \frac{Y_{l,gas} - Y_{l,ghost}}{\delta n} \mp \frac{\delta t\, u_n^2}{2} \frac{\rho_{gas}Y_{l,gas} - \rho_{ghost}Y_{l,ghost}}{\delta n} \tag{121}$$

where $\dot{m}''_l$ is the mass flux of species l per unit area, u_n is the normal component of velocity at the wall pointing into the flow domain, and δn is the distance between the center of the ghost cell and the center of the gas cell. Notice that the last term on the right hand side is subtracted at the predictor step and added at the corrector step, consistent with the biased upwinding introduced earlier.

6.5.6 Density Boundary Condition

Once the temperature and species mass fractions have been defined in the ghost cell, the density in the ghost cell is computed from the equation of state

$$\rho_{ghost} = \frac{p_0}{\mathcal{R}\, T_{ghost}\, \sum_l (Y_{l,ghost}/M_l)} \tag{122}$$

6.6 The Momentum Equation

The three components of the momentum equation are

$$\frac{\partial u}{\partial t} + F_x + \frac{\partial \mathcal{H}}{\partial x} = 0 \quad ; \quad F_x = w\,\omega_y - v\,\omega_z - \frac{1}{\rho}\left(f_x + \frac{\partial \tau_{xx}}{\partial x} + \frac{\partial \tau_{xy}}{\partial y} + \frac{\partial \tau_{xz}}{\partial z}\right) \tag{123}$$

$$\frac{\partial v}{\partial t} + F_y + \frac{\partial \mathcal{H}}{\partial y} = 0 \quad ; \quad F_y = u\,\omega_z - w\,\omega_x - \frac{1}{\rho}\left(f_y + \frac{\partial \tau_{yx}}{\partial x} + \frac{\partial \tau_{yy}}{\partial y} + \frac{\partial \tau_{yz}}{\partial z}\right) \tag{124}$$

$$\frac{\partial w}{\partial t} + F_z + \frac{\partial \mathcal{H}}{\partial z} = 0 \quad ; \quad F_z = v\,\omega_x - u\,\omega_y - \frac{1}{\rho}\left(f_z + \frac{\partial \tau_{zx}}{\partial x} + \frac{\partial \tau_{zy}}{\partial y} + \frac{\partial \tau_{zz}}{\partial z}\right) \tag{125}$$

The spatial discretization of the momentum equations take the form

$$\frac{\partial u}{\partial t} + F_{x,ijk} + \frac{\mathcal{H}_{i+1,jk} - \mathcal{H}_{ijk}}{\delta x} = 0 \tag{126}$$

$$\frac{\partial v}{\partial t} + F_{y,ijk} + \frac{\mathcal{H}_{i,j+1,k} - \mathcal{H}_{ijk}}{\delta y} = 0 \tag{127}$$

$$\frac{\partial w}{\partial t} + F_{z,ijk} + \frac{\mathcal{H}_{ij,k+1} - \mathcal{H}_{ijk}}{\delta z} = 0 \tag{128}$$

where $\mathcal{H}_{ijk}$ is taken at center of cell ijk, u_{ijk} and $F_{x,ijk}$ are taken at the side of the cell facing in the forward x direction, v_{ijk} and $F_{y,ijk}$ at the side facing in the forward y direction, and w_{ijk} and $F_{z,ijk}$ at the side facing in the forward z (vertical) direction. In the definitions to follow, the components of the vorticity ($\omega_x, \omega_y, \omega_z$) are located at cell edges pointing in the x, y and z directions, respectively. The same is true for the off-diagonal terms of the viscous stress tensor: $\tau_{zy} = \tau_{yz}$, $\tau_{xz} = \tau_{zx}$, and $\tau_{xy} = \tau_{yx}$. The diagonal components of the stress tensor τ_{xx}, τ_{xx}, and τ_{xx}; the external force components (f_x, f_y, f_z); and the upwinding bias terms ε_u, ε_v, and ε_w are located at the respective cell faces.

$$\begin{aligned}
F_{x,ijk} = & \left(\frac{1 \mp \varepsilon_w}{2} w_{i+\frac{1}{2},jk}\,\omega_{y,ijk} + \frac{1 \pm \varepsilon_w}{2} w_{i+\frac{1}{2},j,k-1}\,\omega_{y,ij,k-1}\right) \\
& - \left(\frac{1 \mp \varepsilon_v}{2} v_{i+\frac{1}{2},jk}\,\omega_{z,ijk} + \frac{1 \pm \varepsilon_v}{2} v_{i+\frac{1}{2},j-1,k}\,\omega_{z,i,j-1,k}\right) \\
& - \frac{1}{\rho_{i+\frac{1}{2},jk}}\left(f_{x,ijk} + \frac{\tau_{xx,i+1,jk} - \tau_{xx,ijk}}{\delta x} + \frac{\tau_{xy,ijk} - \tau_{xy,i,j-1,k}}{\delta y} + \frac{\tau_{xz,ijk} - \tau_{xz,i,j,k-1}}{\delta z}\right)
\end{aligned} \tag{129}$$

$$\begin{aligned}
F_{y,ijk} = & \left(\frac{1 \mp \varepsilon_u}{2} u_{i,j+\frac{1}{2},k}\,\omega_{z,ijk} + \frac{1 \pm \varepsilon_u}{2} u_{i-1,j+\frac{1}{2},k}\,\omega_{z,i-1,jk}\right) \\
& - \left(\frac{1 \mp \varepsilon_w}{2} w_{i,j+\frac{1}{2},k}\,\omega_{x,ijk} + \frac{1 \pm \varepsilon_w}{2} w_{i,j+\frac{1}{2},k-1}\,\omega_{x,ij,k-1}\right) \\
& - \frac{1}{\rho_{i,j+\frac{1}{2},k}}\left(f_{y,ijk} + \frac{\tau_{yx,ijk} - \tau_{yx,i-1,jk}}{\delta x} + \frac{\tau_{yy,i,j+1,k} - \tau_{yy,ijk}}{\delta y} + \frac{\tau_{yz,ijk} - \tau_{yz,i,j,k-1}}{\delta z}\right)
\end{aligned} \tag{130}$$

$$\begin{aligned}
F_{z,ijk} = & \left(\frac{1 \mp \varepsilon_v}{2} v_{ij,k+\frac{1}{2}}\,\omega_{x,ijk} + \frac{1 \pm \varepsilon_v}{2} v_{i,j-1,k+\frac{1}{2}}\,\omega_{x,i,j-1,k}\right) \\
& - \left(\frac{1 \mp \varepsilon_u}{2} u_{ij,k+\frac{1}{2}}\,\omega_{y,ijk} + \frac{1 \pm \varepsilon_u}{2} u_{i-1,j,k+\frac{1}{2}}\,\omega_{y,i-1,jk}\right) \\
& - \frac{1}{\rho_{ij,k+\frac{1}{2}}}\left(f_{z,ijk} + \frac{\tau_{zx,ijk} - \tau_{zx,i-1,jk}}{\delta x} + \frac{\tau_{zy,ijk} - \tau_{zy,i,j-1,k}}{\delta y} + \frac{\tau_{zz,ij,k+1} - \tau_{zz,ijk}}{\delta z}\right)
\end{aligned} \tag{131}$$

$$\omega_{x,ijk} = \frac{w_{i,j+1,k} - w_{ijk}}{\delta y} - \frac{v_{ij,k+1} - v_{ijk}}{\delta z} \tag{132}$$

$$\omega_{y,ijk} = \frac{u_{ij,k+1} - u_{ijk}}{\delta z} - \frac{w_{i+1,jk} - w_{ijk}}{\delta x} \tag{133}$$

$$\omega_{z,ijk} = \frac{v_{i+1,jk} - v_{ijk}}{\delta x} - \frac{u_{i,j+1,k} - u_{ijk}}{\delta y} \tag{134}$$

$$\tau_{xx,ijk} = \mu_{ijk}\left(2\frac{u_{ijk} - u_{i-1,jk}}{\delta x} - \frac{2}{3}(\nabla \cdot \mathbf{u})_{ijk}\right) \equiv \mu_{ijk}\left(\frac{4}{3}(\nabla \cdot \mathbf{u})_{ijk} - 2\frac{v_{ijk} - v_{i,j-1,k}}{\delta y} - 2\frac{w_{ijk} - w_{ij,k-1}}{\delta z}\right) \tag{135}$$

$$\tau_{yy,ijk} = \mu_{ijk}\left(2\frac{v_{ijk} - v_{i,j-1,k}}{\delta y} - \frac{2}{3}(\nabla \cdot \mathbf{u})_{ijk}\right) \equiv \mu_{ijk}\left(\frac{4}{3}(\nabla \cdot \mathbf{u})_{ijk} - 2\frac{u_{ijk} - u_{i-1,jk}}{\delta x} - 2\frac{w_{ijk} - w_{ij,k-1}}{\delta z}\right) \tag{136}$$

$$\tau_{zz,ijk} = \mu_{ijk}\left(2\frac{w_{ijk} - w_{ij,k-1}}{\delta z} - \frac{2}{3}(\nabla \cdot \mathbf{u})_{ijk}\right) \equiv \mu_{ijk}\left(\frac{4}{3}(\nabla \cdot \mathbf{u})_{ijk} - 2\frac{u_{ijk} - u_{i-1,jk}}{\delta x} - 2\frac{v_{ijk} - v_{ij-1,k}}{\delta y}\right) \tag{137}$$

$$\tau_{xy,ijk} = \tau_{yx,ijk} = \mu_{i+\frac{1}{2},j+\frac{1}{2},k}\left(\frac{u_{i,j+1,k} - u_{ijk}}{\delta y} + \frac{v_{i+1,jk} - v_{ijk}}{\delta x}\right) \tag{138}$$

$$\tau_{xz,ijk} = \tau_{zx,ijk} = \mu_{i+\frac{1}{2},j,k+\frac{1}{2}}\left(\frac{u_{ij,k+1} - u_{ijk}}{\delta z} + \frac{w_{i+1,jk} - w_{ijk}}{\delta x}\right) \tag{139}$$

$$\tau_{yz,ijk} = \tau_{zy,ijk} = \mu_{i,j+\frac{1}{2},k+\frac{1}{2}}\left(\frac{v_{ij,k+1} - v_{ijk}}{\delta z} + \frac{w_{i,j+1,k} - w_{ijk}}{\delta y}\right) \tag{140}$$

$$\varepsilon_u = \frac{u\,\delta t}{\delta x} \tag{141}$$

$$\varepsilon_v = \frac{v\,\delta t}{\delta y} \tag{142}$$

$$\varepsilon_w = \frac{w\,\delta t}{\delta z} \tag{143}$$

The variables ε_u, ε_v and ε_w are local CFL numbers evaluated at the same locations as the velocity component immediately following them, and serve to bias the differencing of the convective terms in the upwind direction. The subscript $i + \frac{1}{2}$ indicates that a variable is an average of its values at the ith and the $(i+1)$th cell. The divergence defined in Eq. (89) is identically equal to the divergence defined by

$$(\nabla \cdot \mathbf{u})_{ijk} = \frac{u_{ijk} - u_{i-1,jk}}{\delta x} + \frac{v_{ijk} - v_{i,j-1,k}}{\delta y} + \frac{w_{ijk} - w_{ij,k-1}}{\delta z} \tag{144}$$

The equivalence of the two definitions of the divergence is a result of the form of the discretized equations, the time-stepping scheme, and the direct solution of the Poisson equation for the pressure.

6.6.1 Force Terms

The external force term components, in addition to including the effects of buoyancy, may also include the drag force from sprinkler droplets.

$$f_{x,ijk} = \frac{1}{2}\frac{\sum \rho C_d \pi r_d^2 (u_d - u_{ijk})|\mathbf{u}_d - \mathbf{u}|}{\delta x\,\delta y\,\delta z} - (\rho_{i+\frac{1}{2},jk} - \rho_\infty)g_x \tag{145}$$

$$f_{y,ijk} = \frac{1}{2}\frac{\sum \rho C_d \pi r_d^2 (v_d - v_{ijk})|\mathbf{u}_d - \mathbf{u}|}{\delta x\,\delta y\,\delta z} - (\rho_{i,j+\frac{1}{2},k} - \rho_\infty)g_y \tag{146}$$

$$f_{z,ijk} = \frac{1}{2}\frac{\sum \rho C_d \pi r_d^2 (w_d - w_{ijk})|\mathbf{u}_d - \mathbf{u}|}{\delta x\,\delta y\,\delta z} - (\rho_{ij,k+\frac{1}{2}} - \rho_\infty)g_z \tag{147}$$

where $\mathbf{g} = (g_x, g_y, g_z)$ is the gravity vector, r_d is the radius of a droplet, $\mathbf{u} = (u_d, v_d, w_d)$ the velocity of a droplet, C_d the drag coefficient, and $\delta x\,\delta y\,\delta z$ the volume of the ijkth cell. The summations represent all droplets within a grid cell centered about the x, y and z faces of a grid cell respectively.

6.6.2 Time Step

The time step is determined by the CFL condition, and in cases of high viscosity, a parabolic stability criterion typical of explicit second order accurate schemes

$$\delta t < \min\left(\frac{\delta x}{u_{ijk}}, \frac{\delta y}{v_{ijk}}, \frac{\delta z}{w_{ijk}}, \frac{\rho_{ijk}\delta x^2}{8\mu_{ijk}}, \frac{\rho_{ijk}\delta y^2}{8\mu_{ijk}}, \frac{\rho_{ijk}\delta z^2}{8\mu_{ijk}}\right) \tag{148}$$

The estimated velocities $u^{(n+1)e}$, $v^{(n+1)e}$ and $w^{(n+1)e}$ are tested at each time step to ensure that the above condition is satisfied. If it is not, then the time step is set to 0.8 of its allowed maximum value and the estimated velocities are recomputed (and checked again). The parabolic stability criterion is only invoked for a DNS calculation.

6.7 The Pressure Equation

The divergence of the momentum equation yields a Poisson equation for the pressure

$$\frac{\mathcal{H}_{i+1,jk} - 2\mathcal{H}_{ijk} + \mathcal{H}_{i-1,jk}}{\delta x^2} + \frac{\mathcal{H}_{i,j+1,k} - 2\mathcal{H}_{ijk} + \mathcal{H}_{i,j-1,k}}{\delta y^2} + \frac{\mathcal{H}_{ij,k+1} - 2\mathcal{H}_{ijk} + \mathcal{H}_{ij,k-1}}{\delta z^2}$$

$$= -\frac{F_{x,ijk} - F_{x,i-1,jk}}{\delta x} - \frac{F_{y,ijk} - F_{y,i,j-1,k}}{\delta y} - \frac{F_{z,ijk} - F_{z,ij,k-1}}{\delta z} - \frac{\partial}{\partial t}(\nabla\cdot\mathbf{u})_{ijk} \tag{149}$$

The lack of a superscript implies that all quantities are to be evaluated at the same time level. This elliptic partial differential equation is solved using a direct (non-iterative) FFT-based solver that is part of a library of routines for solving elliptic PDEs called CRAYFISHPAK [27]. To ensure that the divergence of the fluid is consistent with the definition given in Eq. (10), the time derivative of the divergence is defined

$$\frac{\partial}{\partial t}(\nabla\cdot\mathbf{u})_{ijk} = \frac{(\nabla\cdot\mathbf{u})_{ijk}^{(n+1)e} - (\nabla\cdot\mathbf{u})_{ijk}^{n}}{\delta t} \tag{150}$$

at the predictor step, and then

$$\frac{\partial}{\partial t}(\nabla\cdot\mathbf{u})_{ijk} = \frac{2(\nabla\cdot\mathbf{u})_{ijk}^{n+1} - (\nabla\cdot\mathbf{u})_{ijk}^{(n+1)e} - (\nabla\cdot\mathbf{u})_{ijk}^{n}}{\delta t} \tag{151}$$

at the corrector step. The discretization of the divergence was given in Eq. (89).

Direct Poisson solvers are most efficient if the domain is a rectangular region, although other geometries such as cylinders and spheres can be handled almost as easily. For these solvers, the no-flux condition (152) is simple to prescribe at external boundaries. For example, at the floor, $z = 0$, the Poisson solver is supplied with the Neumann boundary condition

$$\frac{\mathcal{H}_{ij,1} - \mathcal{H}_{ij,0}}{\delta z} = -F_{z,ij,0} \tag{152}$$

However, many practical problems involve more complicated geometries. For building fires, doors and windows within multi-room enclosures are very important features of the simulations. These elements may be included in the overall domain as masked grid cells, but the no-flux condition (152) cannot be directly prescribed at the boundaries of these blocked cells. Fortunately, it is possible to exploit the relatively small changes in the pressure from one time step to the next to enforce the no-flux condition. At the start of a time step, the components of the convection/diffusion term $\mathbf{F}$ are computed at all cell faces that do not correspond to walls. At those cell faces that do correspond to solid walls, prescribe

$$F_n = -\frac{\partial\mathcal{H}^*}{\partial n} + \beta u_n \tag{153}$$

31

where F_n is the normal component of $\mathbf{F}$ at the wall, and β is a relaxation factor empirically determined to be about 0.8 divided by the time step δt. The asterisk indicates the most recent value of the pressure. Obviously, the pressure at this particular time step is not known until the Poisson equation is solved. Equation (153) asserts that following the solution of the Poisson equation for the pressure, the normal component of velocity u_n will be driven closer to zero according to

$$\frac{\partial u_n}{\partial t} \approx -\beta u_n \tag{154}$$

This is approximate because the true value of the velocity time derivative depends on the solution of the pressure equation, but since the most recent estimate of pressure is used, the approximation is very good. Also, even though there are small errors in normal velocity at solid surfaces, the divergence of each blocked cell remains exactly zero for the duration of the calculation. In other words, the total flux into a given obstruction is always identically zero, and the error in normal velocity is usually at least several orders of magnitude smaller than the characteristic flow velocity. When implemented as part of a predictor-corrector updating scheme, the no-flux condition at solid surfaces is maintained remarkably well.

At open boundaries (say $i = I$), $\mathcal{H}$ is prescribed depending on whether the flow is incoming or outgoing

$$\begin{aligned} \mathcal{H}_{I+\frac{1}{2},jk} &= (u_{I,jk}^2 + v_{I,j-\frac{1}{2},k}^2 + w_{I,j-\frac{1}{2},k}^2)/2 \qquad u_{I,jk} > 0 \\ \mathcal{H}_{I+\frac{1}{2},jk} &= 0 \qquad\qquad\qquad\qquad\qquad\qquad u_{I,jk} < 0 \end{aligned} \tag{155}$$

where I is the index of the last gas phase cell in the x direction and $u_{,jk}$ is the x component of velocity at the boundary. The value of H in the ghost cell is

$$\mathcal{H}_{I+1,jk} = 2\mathcal{H}_{I+\frac{1}{2},jk} - \mathcal{H}_{I,jk} \tag{156}$$

6.8 Particle Tracking

Thermal elements are introduced into the flow field as a means of introducing heat and as a way to visualize the flow. The position $\mathbf{x}_p$ of each thermal element is governed by the equations

$$\frac{d\mathbf{x}_p}{dt} = \mathbf{u} \tag{157}$$

The thermal element positions are updated according to the same predictor-corrector scheme that is applied to the other flow quantities. Briefly, the position $\mathbf{x}_p$ of a given thermal element is updated according to the two step scheme

$$\mathbf{x}_p^{(n+1)e} = \mathbf{x}_p^n + \delta t\, \bar{\mathbf{u}}^n \tag{158}$$

$$\mathbf{x}_p^{n+1} = \frac{1}{2}\left(\mathbf{x}_p^n + \mathbf{x}_p^{(n+1)e} + \delta t\, \bar{\mathbf{u}}^{(n+1)e}\right) \tag{159}$$

where the bar over the velocity vector indicates that the velocity of the fluid is interpolated at the element's position.

7 Conclusion

The equations and numerical algorithm described in this document form the core of an evolving fire model. As research into specific fire-related phenomena continues, the relevant parts of the model can be improved. Because the model was originally designed to analyze industrial scale fires, it can be used reliably when the fire size is specified and the building is relatively large in relation to the fire. In these cases, the model predicts flow velocities and temperatures to an accuracy of 10 to 20% compared to experimental measurements. Currently, research is focussed on improving both the gas phase and solid phase descriptions of combustion in the model so that simulations involving fire growth and suppression, especially in residential sized rooms, can be improved.

Any user of the numerical model must be aware of the assumptions and approximations being employed. There are two issues for any potential user to consider before embarking on calculations. First, for both real and simulated fires, the growth of the fire is very sensitive to the thermal properties of the surrounding materials. Second, even if all the material properties are known, the physical phenomena of interest may not be simulated due to limitations in the model algorithms or numerical grid. Except for those few materials that have been studied to date at NIST, the user must supply the thermal properties of the materials, and then validate the performance of the model with experiments to ensure that the model has the necessary physics included. Only then can the model be expected to predict the outcome of fire scenarios that are similar to those that have actually been tested.

8 Nomenclature

A_s	water droplet surface area
B	pre-exponential factor for Arrhenius reaction
C	Sprinkler C-Factor
C_D	drag coefficient
C_s	Smagorinsky constant (LES)
c_p	constant pressure specific heat
D	diffusion coefficient
D^*	characteristic fire diameter
d_m	median volumetric droplet diameter
E	activation energy
$\mathbf{f}$	external force vector (excluding gravity)
g	acceleration of gravity
$\mathcal{H}$	total pressure divided by the density
h	enthalpy; heat transfer coefficient
h_i	enthalpy of ith species
k	thermal conductivity; suppression decay factor
M	molecular weight of the gas mixture
M_i	molecular weight of ith gas species
$\dot{m}_w''$	water flux per unit area
m_w''	water mass per unit area
Nu	Nusselt number
Pr	Prandtl number
p	pressure
p_0	background pressure
$\tilde{p}$	pressure perturbation
$\dot{q}'''$	heat release rate per unit volume
$\dot{q}_f''$	fire heat release rate per unit area
$\dot{q}_r''$	radiative flux to a solid surface
$\dot{q}_c''$	convective flux to a solid surface
$\dot{q}_{rr}''$	radiative loss from a solid surface
$\dot{q}_w''$	water cooling per unit area
$\mathcal{R}$	universal gas constant
Re	Reynolds number
r_d	water droplet radius
RTI	Response Time Index of sprinkler
S	deformation tensor
Sc	Schmidt number
T	temperature
t	time
t_b	thermal element burn-out time (LES)
$\mathbf{u} = (u, v, w)$	velocity vector
$\dot{W}_i'''$	production rate of ith species per unit volume
We	Weber number
$\mathbf{x} = (x, y, z)$	position vector
Y_i	mass fraction of ith species
γ	ratio of specific heats

ΔH	heat of combustion
δ	wall thickness
ε	emissivity
κ	absorption coefficient
μ	dynamic viscosity
ν_i	stoichiometric coefficient
ρ	density
τ	viscous stress tensor
χ_r	radiative loss fraction
χ_s	smoke or soot yield
σ	Stefan-Boltzmann constant
$\omega = (\omega_x, \omega_y, \omega_z)$	vorticity vector

References

[1] H.C. Hottel. Stimulation of Fire Research in the United States After 1940. *Combustion Science and Technology*, 39:1–10, 1984.

[2] J. Quintiere. A Perspective on Compartment Fire Growth. *Combustion Science and Technology*, 39:11–54, 1984.

[3] G.P. Forney and W.F. Moss. Analyzing and Exploiting Numerical Characteristics of Zone Fire Models. *Fire Science and Technology*, 14:49–60, 1994.

[4] S.V. Patankar. *Numerical Heat Transfer and Fluid Flow*. Hemisphere Publishing, New York, 1980.

[5] R.G. Rehm and H.R. Baum. The Equations of Motion for Thermally Driven, Buoyant Flows. *Journal of Research of the NBS*, 83:297–308, 1978.

[6] H.R. Baum and K.B. McGrattan. Simulation of Large Industrial Outdoor Fires. In *Fire Safety Science – Proceedings of the Sixth International Symposium*. International Association for Fire Safety Science, 1999.

[7] J. Smagorinsky. General Circulation Experiments with the Primitive Equations. I. The Basic Experiment. *Monthly Weather Review*, 91:99–164, 1963.

[8] J.W. Deardorff. Numerical Investigation of Neutral and Unstable Planetary Boundary Layers. *Journal of Atmospheric Sciences*, 29:91–115, 1972.

[9] M. Germano, U. Piomelli, P. Moin, and W.H. Cabot. A Dynamic Subgrid-Scale Eddy Viscosity Model. *Physics of Fluids A*, 3:1760–1765, 1991.

[10] D.K. Lilly. A Proposed Modification of the Germano Subgrid-Scale Closure Method. *Physics of Fluids A*, 4:633–635, 1992.

[11] H.R. Baum, K.B. McGrattan, and R.G. Rehm. Three Dimensional Simulations of Fire Plume Dynamics. *Journal of the Heat Transfer Society of Japan*, 35:45–52, 1997.

[12] R.C. Reid, J.M. Prausnitz, and B.E. Poling. *Properties of Gases and Liquids*. McGraw-Hill, Inc., New York, 4th edition, 1987.

[13] A. Atreya and S. Agrawal. Effect of Heat Loss on Diffusion Flames. *Combustion and Flame*, 115:372–382, 1998.

[14] H.R. Baum and B.J. McCaffrey. Fire Induced Flow Field – Theory and Experiment. In *Fire Safety Science – Proceedings of the Second International Symposium*, pages 129–148. International Association for Fire Safety Science, 1989.

[15] I.K. Puri and K. Seshadri. Extinction of Diffusion Flames Burning Diluted Methane and Diluted Propane in Diluted Air. *Combustion and Flame*, 65:137–150, 1986.

[16] C.K. Westbrook and F.L. Dryer. Simplified Reaction Mechanisms for the Oxidation of Hydrocarbon Fuels in Flames. *Combustion Science and Technology*, 27:31–43, 1981.

[17] J.P. Holman. *Heat Transfer*. McGraw-Hill, New York, 5th edition, 1989.

[18] G. Heskestad and R.G. Bill. Quantification of Thermal Responsiveness of Automatic Sprinklers Including Conduction Effects. *Fire Safety Journal*, 14:113–125, 1988.

[19] M. DiMarzo. The Effect of Minute Water Droplets on a Simulated Sprinkler Link Thermal Response. Technical report, University of Maryland, 1999.

[20] T.S. Chan. Measurements of Water Density and Droplet Size Distributions of Selected ESFR Sprinklers. *Journal of Fire Protection Engineering*, 6(2):79–87, 1994.

[21] H.Z. Yu. Investigation of Spray Patterns of Selected Sprinklers with the FMRC Drop Size Measuring System. In *Fire Safety Science – Proceedings of the First International Symposium, International Association For Fire Safety Science*, pages 1165–1176, 1986.

[22] A. Hamins and K.B. McGrattan. Reduced-Scale Experiments to Characterize the Suppression of Rack Storage Commodity Fires. Technical Report NIST Internal Report (NISTIR 6439), National Institute of Standards and Technology, Gaithersburg, Maryland 20899, 1999.

[23] H.Z. Yu, J.L. Lee, and H.C. Kung. Suppression of Rack-Storage Fires by Water. In *Fire Safety Science – Proceedings of the Fourth International Symposium, International Association For Fire Safety Science*, pages 901–912, 1994.

[24] K.B. McGrattan, R.G. Rehm, and H.R. Baum. Fire-Driven Flows in Enclosures. *Journal of Computational Physics*, 110(2):285–292, 1994.

[25] H.R. Baum, O.A. Ezekoye, K.B. McGrattan, and R.G. Rehm. Mathematical Modeling and Computer Simulation of Fire Phenomenon. *Theoretical and Computational Fluid Dynamics*, 6:125–139, 1994.

[26] G. Continillo, F.M Denaro, and F.S. Marra. Accuracy and Stability Analysis of Time-Integrated Schemes for Advection-Diffusion-Reaction Equations. In *Seventh International Conference on Numerical Combustion*, page 99, 1998.

[27] Green Mountain Software, Boulder, Colorado. *CRAYFISHPAK User's Guide, Cray Version 1.1*, 1990.